

The SparSpec algorithm and the application to the detection of spatial periodicities in tokamaks: from a 1D to a 2D analysis

[note: this work is partially based on a 4th year bachelor project by one of the authors (JCE), performed while being a student at the SPC-EPFL under the supervision of the corresponding author (DTA)]

D.Testa¹ (ORCID ID: 0000-0002-6372-882X), J.Charrière¹

¹Ecole Polytechnique Fédérale de Lausanne (EPFL), Swiss Plasma Center (SPC), CH-1015 Lausanne, Switzerland
e-mail address of corresponding author: duccio.testa@epfl.ch

A well-known, previously only 1D, algorithm using the Sparse Representation of Signals and an iterative Block Coordinate Descent method (the SparSpec-1D algorithm) has been further developed and tested in a 2D spatial domain to obtain the toroidal and poloidal periodicities of magnetic fluctuations in a tokamak. The tests are performed essentially using simulated data, because *we know what the answer must be*, and therefore it is straightforward to verify the accuracy of the algorithm. Two more examples using actual data from the JET and TCV tokamaks are considered to test the algorithm in real-life experiments; a further example using simulated data constructed from nominal test cases for the forthcoming ITER tokamak is also considered. The CPU run-time and the precision of the SparSpec-2D algorithm are studied as function of different analysis parameters. The stability of the algorithm is also tested via the introduction of random errors in the input signal. We find that the spatial-2D version of the baseline SparSpec-1D algorithm accurately finds the modes in the 2D toroidal and poloidal space, provided the set of magnetic sensors used for the analysis do not have a (quasi-)ignorable coordinate. The number of probes and their position are the key parameters that must be optimized for finding correct solutions. The main difficulty, as for the baseline SparSpec-1D algorithm, lies in dealing correctly with the intrinsic measurement uncertainties associated to the input magnetic fluctuation data, particularly the phase error, and this has been already separately reported in a companion work. However, the required CPU run-time for SparSpec-2D is significantly longer than that needed for 2x SparSpec-1D, and thus SparSpec-2D is effectively suitable for use only when the 2x 1D analyses cannot provide accurate results, which is the case when the set of measurements does not have an ignorable coordinate.

Keywords: Sparse Representation of Signals, SparSpec algorithm, mode analysis in tokamaks.

1. Introduction.

Detecting the temporal periodicities in a time series is a routine task in many fields of science, the Fourier Transform (FT) being the standard tool when regular sampling is obtained. More problematic is the detection of these temporal frequencies when the time series is irregularly sampled. However, this is a rather common difficulty in astronomy and many algorithms have been devised for this task [1-13]. Following up from extensive previous work on tokamak plasmas, here we will consider the application of one of them, the SparSpec Algorithm (previously discussed at length in [1-3, 14, 15]) to the detection of 2D spatial periodicities in such plasmas.

The SparSpec code is based on the theory of the *Sparse Representation of Signals* (SRS) (for further details see <http://userpages.irap.omp.eu/~hcarfantan/SparSpec1.4/SparSpec.html.html>). Its simplest version, dubbed *SS-H2*, and its application to the analysis of 1D spatial periodicities in tokamaks has been presented multiple times [3, 16-26]. In a companion work [1] we presented a first development of the baseline SparSpec algorithm SS-H2 as applied to the detection of spatial periodicities in tokamaks, namely using the measurement uncertainties to weight the data, the spectral window and thus the penalization criterion. This is the *SS-V5v0*¹ version of the SparSpec-1D algorithm. A second development [2] (the full SS-V5 version of the SparSpec-1D algorithm) aims at presenting the use of a *memory with relaxation* (MwR) scheme to provide better input constraints for the analysis and, therefore, speed up and achieve a higher accuracy in the real-time (RT) calculations. The third development, namely the extension of SS-H2 to a 2D spatial problem, is reported in this work.

Magnetic fluctuations are a very common feature of thermonuclear fusion plasmas and, in addition to their frequency analysis, it is important to determine their spatial structure, namely (considering the specific case of a tokamak device) their decomposition in toroidal and poloidal harmonics. When the magnetic probes used for the measurement of these fluctuations are equi-spaced and arranged in arrays which have a constant toroidal or poloidal coordinate (this then being the *ignorable* coordinate, while the other is the coordinate along which the spatial analysis is performed, i.e. the *non-ignorable* coordinate), the system can be treated as the superposition of independent 1D equations. Note that the definition of an ignorable coordinate provided above strictly applies only in the very common situation of an idealized tokamak, i.e. completely axisymmetric. In the presence of long-lived and global modes (such as $m=2/n=1$ tearing modes, for instance), or error fields, or externally driven magnetic perturbations, then the equilibrium is no more axisymmetric. Therefore, truly ignorable coordinates do not exist any longer, hence a generalization to “quasi-ignorable” coordinates is needed.

¹The acronym SS-V5v0 is used here for consistency with the companion submissions presenting the results of including in SparSpec-1D first [1] solely the measurement uncertainties and the ensuing error weighting, and then [2] a memory with relaxation scheme: v is the parameter defining the primary memory scheme, and thus SS-V5v0 is the version of the SparSpec-V5 algorithm which uses the error weighting but runs without the memory, $v=0$.

For systems with (quasi-)ignorable coordinates, the Nyquist criterion can then be used to obtain the spatial periodicities of the signals along the non-ignorable coordinate using a spatial Discrete Fourier Transform (DFT), with the limitation of the Nyquist value giving a maximum (toroidal, poloidal) mode number $\text{MaxMode}\{\text{NN}, \text{MM}\}$ that can be detected. This is indeed the usual situation in many currently operating (tokamak) fusion devices. However, when such arrangements of magnetic sensors are not possible due to installation constraints, or have been lost due to sensors' failures, then either:

- (a) the analysis is only performed using the surviving subset of equi-spaced sensors along the original non-ignorable coordinate, thus very likely reducing the value of $\text{MaxMode}\{\text{NN}, \text{MM}\}$, possibly significantly, with clear detrimental consequences on the results; or
- (b) a different set of sensors has to be used, for which both toroidal and poloidal coordinates may become concurrently non-ignorable and the DFT cannot be used as the sensors are no more equi-spaced in such a 2D geometrical arrangement; note that this might also be the starting point for the device, before any loss of sensors, if equi-spaced arrangements of sensors with an ignorable coordinate cannot be installed.

To tackle this problem, we now wish to adapt the SparSpec-1D algorithm, which was specifically developed to treat the case of non-uniformly spaced sensors with an ignorable coordinate, to a 2D spatial system, i.e. where both coordinates are by default concurrently non-ignorable. Specifically, we consider applications of the SparSpec-2D algorithm to the future ITER, DTT and DEMO tokamaks, particularly in view of their intended long-term operation, when sensors' failure may become unavoidable, and stellarators, which are intrinsically characterised by a multi-dimensional spatial topology such that ignorable coordinates cannot generally be found. However, for simplicity we consider in this work only the application to currently operating tokamak fusion devices, such as JET and TCV, where SparSpec-1D is already routinely deployed for magnetic fluctuation analyses, both RT and post-pulse, and to ITER, where extensive analyses of simulated data using the SparSpec-1D algorithm have already been performed [17, 27].

This paper is organised as follows. The mathematical foundations of the SRS and of the *SparSpec-1D* code have been presented elsewhere multiple times, hence in Section-2 we will only very briefly review the main details needed for the following sections of this work. Section-3 will then present the mathematical approach taken to extend the baseline version of the SparSpec-1D algorithm (i.e. SS-H2) to a 2D spatial coordinate system, this version being dubbed *SS-2D*. Section-4 will then compare the results obtained with SS-2D for a few illustrative test cases based on simulated data. Section-5 then shows the application of SS-2D using actual data from the JET and TCV tokamaks, while in Section-6 we consider simulated data for the forthcoming ITER tokamak. Section-7 will then present our conclusions and a brief sketch of the currently envisaged further development of the

SparSpec algorithm, for application to other complex engineering and scientific systems such, as an example, quasi-RT data analysis for the ITER tokamak.

2. The Sparse Representations of Signals and the SparSpec-1D algorithm: a (very) brief review.

Since this is a follow-up contribution from a previous two-part work [1,2] by the same corresponding author, the Readers are referred to these two papers, to [3] and to the references therein for extensive details on SS-H2, while here we present essentially only a brief reminder for ease of reading.

The SparSpec algorithm solves the penalized least-square criterion

$J(\mathbf{x}) = \frac{1}{2} \ \mathbf{y} - W\mathbf{x}\ _2^2 + \lambda R(\mathbf{x}),$	(1a)
---	------

where $[\mathbf{y}]^2$ is the vector of measurements, $[[W]]$ is the spectral window of the system, $[\mathbf{x}]$ are the pulsation modes, λ is a relaxing parameter, and $R(\mathbf{x})$ is the L1-norm of the penalization function $[R(\mathbf{x})]$. In eq.(1a) and following, the subscript $\|\dots\|_k$ indicates the Lk-norm, namely L1 (for k=1) and L2 (for k=2). Many different $[R(\mathbf{x})]$ have been employed to address the minimization procedure: the L1-norm is typically used by the SparSpec algorithm. Equation (1a) then reads:

$J(\mathbf{x}) = \frac{1}{2} \ \mathbf{y} - W\mathbf{x}\ _2^2 + \lambda \ \mathbf{x}\ _1.$	(1b)
--	------

The relaxing parameter λ plays a major role in our discussion since it is related to the *freedom* that we allow in the criterion to choose how many components to pick: the higher the value of λ , the fewer components $\{\mathbf{x}\}$ we are allowing to fit $[\mathbf{y}]$ within the measurement constraints provided by $[[W]]$.

Since the L1-norm is not-differentiable at zero, SparSpec uses a modified version of an iterative Block Coordinate Descent (BCD) method [28], which is based on subsequent scalar minimization steps for the complex-valued k-th component of the vector $[\mathbf{x}]$ and is combined with an Iterative Reweighted Least-Squares (IRLS) method to ensure that (a) $J(\mathbf{x})$ does not grow over the different iterations, and (b) if a component of the spectrum is zero at the iteration t, it will also remain zero at the iteration t+1. One of the features of this procedure is the low computational cost of each iterative step.

3. From SparSpec-1D to SparSpec-2D: definition of the input signal and of the spectral window.

²Note that here for the in-line and un-numbered equations in the text (but not for those in separate and numbered boxes) we will always use the notation $[\mathbf{x}]$ to designate a vector \mathbf{x} , the notation $[[\mathbf{x}]]$ to designate a matrix \mathbf{x} and the notation $\{\mathbf{x}\}$ to designate an ensemble of elements \mathbf{x} .

To carry out the analysis of the accuracy and numerical performance of the SS-2D algorithm, an adequate signal vector S_{IN} must be built, to closely mimic the actual measurements made in a tokamak device. To this end, we consider a complex-valued signal³ measured by the magnetic probes at the coordinate $\{\phi, \theta\}_k$ where $\{\phi, \theta\}$ are the toroidal and poloidal angular coordinates of the k -th sensor, respectively. In currently operating (JET, TCV), and future (ITER, DTT, DEMO) tokamak devices the total number of sensors is of the order of $10 \rightarrow 50$. Finally, to the nominal/exact 1D (spatial) matrix⁴ $[y] = [[W]] * [x]$ appearing in eqs.(1a,1b) we need to add various sources of errors (here again we follow exactly the definitions presented in [1,2], to which the Readers are referred to for further details, in particular all σ 's appearing here represent a relative error):

1. the total instrumental error σ_k , which can be up to 15% of the total signal;
2. the time delay δ_k between the local measurement made by the sensor and the corresponding value acquired and stored in the data system;
3. the error $\sigma_{n,m}$ in the determination of the Fourier coefficients, which can also be up to 15% of the total signal.

As a result, a final expression for the signal vector at the time point t_p can be proposed as follows:

$S_0(\{\phi, \theta\}_k) = \sum_{l=-L_{MAX}}^{L_{MAX}} W_{l,\{k\}} * x_l = \sum_{\{n,m\}=-\{N_{MAX}, M_{MAX}\}}^{+\{N_{MAX}, M_{MAX}\}} x_{n,m} \exp(in\phi_k + im\theta_k). \quad (2a)$	
$S_{IN}(\{\phi, \theta\}_k) = \left\{ \sum_{\{n,m\}=-\{N_{MAX}, M_{MAX}\}}^{+\{N_{MAX}, M_{MAX}\}} \left[x_{n,m} (1 + \sigma_{\{n,m\}}) \right] \exp(in\phi_k + im\theta_k) \right\} \times (1 + \sigma_k) \exp(i\pi\delta_k) \quad (2b)$	

In eq.(2a) $S_0(\{\phi, \theta\}_k)$ is the nominal 2D input signal at the k -th sensor, not accounting for measurement uncertainties nor phase shifts, while $S_{IN}(\{\phi, \theta\}_k)$ appearing in eq.(2b) is the 2D signal as actually measured, which includes all sources of errors and a phase shift. We can now use this latter analytical form of $S_{IN}(\{\phi, \theta\}_k)$ to produce numerically a set of realistic input signals with which we can run our SS-2D simulations.

To use the same algorithm as in SS-H2, the 2D problem cast from eq.(2b) has to be written in the same way as that cast in eq.(1b). If we have a set of signals y_k that are located at different angles $\{\phi, \theta\}_k$ we can already express the vector $[y]$ and we know the value of each $\{\phi_k, \theta_k\}$ at each line (and column) of $[[W_{2D}]] = [[\exp(in\phi + im\theta)]]$. For convenience, from this point onward we now label

³As we consider only the spatial decomposition, our *input measured* signal corresponds in fact to the temporal Fourier Transform, at any one specified frequency up to the Nyquist value $f_s = 1/(2\tau_s)$, of the raw real-valued voltage signal that is actually acquired by the probes at the sampling time τ_s .

⁴It is clear what we want to achieve from a mathematical and theoretical point of view: if we can reformulate the 2D (ϕ, θ) problem *exactly* as a 1D (ψ) problem through some appropriate pre- and/or post-processing algebraic manipulations, then on the computational side we could run *almost exactly* the core module of SparSpec-1D (i.e. SS-H2) also for a 2D analysis.

$\{\phi_k, \theta_k\} \equiv \{\psi\}_k$, keeping however the $\{n, m\}$ notation for clarity of presentation. We can then find an ordering in the overall 2D spatial periodicities, namely we can determine the subset of toroidal $\{i, p\} \in \{N_{MAX}\}$ and poloidal $\{j, q\} \in \{M_{MAX}\}$ indexes defining the spatial $\{n_i, m_j\}$ modes such that $n_i^2 + m_j^2 > n_p^2 + m_q^2$. The resulting 2D spectral window $[[W_{2D}]]$ is no more a Toeplitz matrix, as for the 1D case, but otherwise the SparSpec-1D algorithm (actually in any of its version, i.e. SS-H2 and also SS-V5) can be directly applied in 2D with a modified implementation of the BCD algorithm (and similarly for the error and the memory for SS-V5) that accounts for the above sorting of the {toroidal, poloidal} components.

4. A few selected test cases for the SparSpec algorithms SS-2D.

For clarity of presentation and ease of reading, in this Section we present a very limited number of selected test cases in order to illustrate the main features and the success vs. failures of the SS-2D algorithm. In the next section we will then focus on a thorough statistical analysis using an extensive number of simulated test cases. It is clear that multiple parameters need to be set to determine the accuracy and speed of SS-2D.

First, the input signal $S_{IN}(\psi_k)$ must be generated, and this is determined by the number $=N_{SENS}$ (labelled K above) and the spatial distribution $= \{\text{random, equi-spaced}\}$ of the sensors. The peculiarity of the 2D analyses lies on the role of the ignorable coordinate, therefore we can consider two generic 2D arrangements of sensors which are differentiated by the presence or absence of a subset (and possibly the full set) of sensors for which one of the two coordinates $\{\phi, \theta\}$ is alternatively ignorable. The first case is dubbed *orthogonal sensors*, i.e. a subset exists for which an ignorable coordinate can be found, while the second case corresponds to *non-orthogonal sensors*. The orthogonality condition is only valid within the installation tolerances, typically $\sim \pm 3\text{deg}$ at the most⁵. Therefore, (as an example) ϕ is the ignorable coordinate for the subset of sensors all located at $\phi = \phi_0 \pm 3\text{deg}$ but at a different poloidal position.

To clarify what we intend by *orthogonal sensors*, fig1(a,b,c) shows three illustrative examples of the actual 2D positions of the high-frequency (HF) magnetic sensors in existing and forthcoming tokamak devices, namely in TCV (fig1a), in JET (fig1b) and as currently intended for ITER (fig1c). In TCV we have 38x Mirnov sensors each in four poloidal arrays separated by $\pi/2$ toroidally; we then have

⁵Since the positional error is a function of machine size at the wall, a $\pm 3\text{deg}$ angular error would correspond to $\sim 20\text{cm}$ in ITER, for instance, which is clearly unrealistically large. However, and as explained in previous SparSpec literature, this maximum $\pm 3\text{deg}$ angular error also includes the positional error that corresponds to uncertainties in the end-to-end calibration of the acquisition line. Thus, this very large value for the angular error is used for consistency with previous literature, with the purpose of showing that even in this extreme case the accuracy of all variants of the SparSpec algorithm remains sufficient.

17x Mirnov sensors each in three toroidal arrays on the low-field-side (LFS), and 8x Mirnov sensors each, in three toroidal arrays on the high-field-side (HFS): the LFS and HFS toroidal arrays sit at three different vertical, hence poloidal, positions. For the LFS arrays, 16 sensors are exactly equi-spaced by $\pi/8$ toroidally, and the 17th sensors sits between two of them; for the HFS arrays the sensors are exactly equi-spaced by $\pi/4$ toroidally. Unfortunately, in TCV none of these 10 arrays is such that both coordinates are not ignorable, and thus all the individual toroidal arrays are exactly orthogonal to all the individual poloidal arrays. As it will transpire later, this is a major drawback for 2D spatial analyses, for which the only effective solution is to combine subsets of toroidal and poloidal sensors from different arrays, with the problem that these sensors then might have a different intrinsic measurement error⁶ or be at a very different distance from the LCFS. The latter is a problem particularly important in TCV, where the wall is almost never conformal to the LCFS due to the large variety of possible plasma shapes, and which is usually further compounded by the strong ballooning physics (that is: a very strong variation of the poloidal mode amplitude on the LFS, see fig.20 in [29] for a specific example of this). In TCV we also have 3x LTCC-3D magnetic sensors [29], which sit at Z=-115mm in three not equi-spaced toroidal sectors, thus somewhat in between some of the Mirnov sensors on the LFS. The LTCC-3D data are acquired at a different frequency (2MHz compared to 500kHz for the Mirnov sensors), and thus it is not straightforward to use them together with a suitably selected subset of Mirnov sensors.

In JET (see fig1b), some of the HF magnetic sensors (the H-coils) are positioned very close to each other to form a high-resolution array: if all the 8x H-coils are used concurrently, there is no more an ignorable coordinate, and therefore this array becomes well suited for combined toroidal and poloidal analyses. Furthermore, since in JET the wall is typically conformal to the LCFS, ballooning physics plays a much less significant role.

The ITER device (se fig1c) follow a mixed approach: most of the sensors are distributed in quasi-exactly orthogonal arrays as in TCV (for instance, those highlighted by the *red* and *blue* contours in fig1c), but subsets of sensors can be found for which both coordinates are not-ignorable, as in JET (for instance, those highlighted with the *green* contours in fig1c).

Second, we need to consider the number of sensors = N_{SENS} and their spatial distribution. As we mostly use SparSpec for the analysis of magnetic fluctuations in JET, TCV and ITER, and the number of magnetic sensors available for any such analyses in these devices range from ~ 10 to ~ 50 , which typically are not solely equi-spaced, we set a fixed $N_{\text{SENS}}=40$ for simplicity and allows uniformly or randomly distributed sensors. In terms of the $\{\phi, \theta\}$ angular coordinate of the sensors, we allow to

⁶And then we will need to use SparSpec-V5(v0) to account for this in a 2D operational space, which is our next, and most likely final, intended development of the SparSpec algorithm.

have them quasi-exactly orthogonal, i.e. half the sensors are at $\phi=\{0,\pi\}$ with varying θ (within the nominal installation tolerances of $\sim 3\text{deg}$, this would then be the classic 1D poloidal array), while the other half is at $\theta=\{0,\pi\}$ with (similarly) varying ϕ (the classic 1D toroidal array), or completely non-orthogonal, i.e. both $\{\phi,\theta\}$ angular coordinate vary.

Third, we need to consider the number of non-zero input signal components $=\{N,M\}_{\text{COMP}}$. Magnetic fluctuations can be spatially analysed starting from a time series, hence multiple signal components are present, or at individual mode frequencies (=Eigenmodes), hence typically only one component is present. Furthermore, and essentially due to the toroidal geometry, for any spatial component the toroidal mode number is a good quantum number, i.e. it is conserved throughout the radial cross-section of the tokamak, while the poloidal harmonic content may significantly change, from one single harmonic at the mode resonant surface to multiple harmonics at the plasma edge, i.e. essentially where the magnetic sensors make the measurements. Therefore, we must consider the general case of $N_{\text{COMP}}=1 \rightarrow 5$ with $M_{\text{COMP}}=1 \rightarrow 5$ for each individual value of N_{COMP} .

Fourth, we need to consider the value of $\{N,M\}_{\text{MAX}}$: this is set to $N_{\text{MAX}}=15$ and $M_{\text{MAX}}=35$ to cover not only existing, but also the generic (toroidal, poloidal) case of future tokamaks such as ITER.

Finally, we need to set (a) the (randomly chosen) values for the non-zero input components (namely the corresponding spatial mode numbers and amplitudes), thus determining the input set $\{\mathbf{x}\}$; and (b) the randomly distributed phase shifts $\{\delta_k\} \in [0 \rightarrow 1] \times \pi$ and the relative errors $\{\sigma_k, \sigma_l\} \in [0 \rightarrow 1] \times 0.15$.

Then, we need to define the analysis parameters required by the SparSpec-2D algorithm, in addition to $\lambda_{\text{REL}} \in [0 \rightarrow 1]$ such that $\lambda = \lambda_{\text{REL}} * \lambda_{\text{MAX}}$, where $\lambda_{\text{MAX}} = \max([\mathbf{W}][\mathbf{y}])$:

- The numerical set of *atoms* (namely: the set of functions that model $\{\mathbf{x}\}$) used to find the solutions: this must be sparse, and it is practically limited to $\leq |\text{FmaxS}|$ only by RAM and CPU resources; following previous analyses, we set $\text{FmaxS}\{N,M\} = 5 \times \{N,M\}_{\text{MAX}}$.
- Since the solution set is sparse, it is possible that spurious, very-low amplitude elements are found due to the presence of noise in the input signal; these can be removed by defining a cut-off value below which the amplitude of these spurious solutions is set to $=0$; this cut-off value is linked to the overall measurement uncertainties $\sigma_{\text{TOT}}(\psi_k) = |\text{SIN}(\psi_k) - \text{S}_0(\psi_k)|$.
- We set the total number of iterations allowed for convergence of the BCD algorithm $n_{\text{IT}}=1000$ and the relative tolerance threshold for checking the convergence conditions $\text{TR}_{\text{IT}} = 1 \times 10^{-5}$.
- As we randomize many analysis parameters at each individual simulation, for each value of N_{COMP} we need to run the analysis $N_{\text{ITER}}=O(10^4)$ and calculate the RMS and STD value of our output results so as to obtain a statistically significant performance analysis of the SS-2D algorithm.

Our MATLAB routine randomly chooses K locations for the probes, the different spatial frequencies

(modes) and their amplitude to avoid any bias in the evaluation of the SS-2D algorithm. The data that will be compared to assess the accuracy and the speed of the SS-2D algorithm are the average elapsed time and the number of iterations needed to converge, the relative error on the input vs. output energy conservation, and the number of errors made in the result (hereafter, we will call them faults⁷). Note that the accounting of the faults is bi-directional, i.e. we consider both (a) the input components which are not correctly found in the output and also (b) the non-zero (within the measurement errors) output components that do not exist in the input. The required CPU run-time has been evaluated using the MATLAB function *timeit*, which returns the relative and system-dependent clock time taken by the computer to perform the calculations with different algorithms.

As illustrative examples, fig2 and fig3 show two single test runs, always using $N_{\text{COMP}}=3=M_{\text{COMP}}$, $\lambda_{\text{REL}}=0.15$ and $N_{\text{SENS}}=40$ randomly spaced sensors. While in fig2 the sensors are quasi-orthogonally distributed, thus with one (quasi-)exactly ignorable coordinate, i.e. as the TCv and the most common arrangement in ITER, in fig3 the sensors are purely randomly distributed, similarly in a sense to randomly selecting a subset of the sensors in JET and ITER shown in fig1b and fig1c, respectively. In fig2 the quasi-exact orthogonality condition is implemented by setting $N_{\text{SENS}}/2=20$ sensors at $\phi=\pi\pm\Delta\psi_{\text{IT}}$, and the other 20 sensors at $\theta=\pi\pm\Delta\psi_{\text{IT}}$, where $\Delta\psi_{\text{IT}}=(3/180)\times\pi$ is the nominal angular installation tolerance, randomly distributed between the relevant subset of sensors.

Even in the non-optimal situation of quasi-orthogonal sensors illustrated by fig2, SS-2D detects rather well the input modes, with a minimal relative error on the overall energy conservation =0.22, but at the high computational cost $\tau_{2D}\sim 26\text{msec}$, corresponding to 29 iterations of the algorithm. Compare however the 2D with the 2x1D separate {toroidal, poloidal} results shown in fig2b: the accuracy is similar, but the computational time is much shorter, respectively $\tau_{1D}\sim 0.09\text{msec}$ and $\tau_{1D}\sim 0.08\text{msec}$ for a similar number of iteration (22 and 23 for the toroidal and poloidal analyses, respectively). From this single test run, it would seem absolutely clear that for (quasi-)orthogonal sensors SS-2D does not bring about any real advantage with respect to running separately twice SS-H2.

Looking now at the optimal 2D case of non-orthogonal sensors illustrated by fig3, SS-2D does indeed very well in detecting the input modes, however at the significant computational cost $\tau_{2D}\sim 20\text{msec}$ for 10 iterations, while SS-H2 quite significantly fails, as expected, even if the computational cost is rather small and the amplitude of some of the input modes is at least partially correctly recovered. Solely from this single test run, one could conclude that SS-2D is very accurate, even if not very fast,

⁷We choose to directly relate the accuracy (or lack of) to the number of faults that have been made by the minimization routine, the faults being the number of mismatching components between the true vector and the one resulting from the minimization procedure: clearly, the higher the number of mismatches in the components, the lower the accuracy.

for a truly 2D set of (magnetic) sensors and should be used preferentially to running twice SS-H2 for such an arrangement of sensors.

The much longer CPU run-time for SS-2D is not at all surprising and has a practical reason to begin with: in a 1D case, at each iteration of the BCD algorithm the solution is sought scanning a set of atoms of length $L_{1D}=2 \times F_{\max} S \{N, M\} + 1$, while in 2D we have to scan a much bigger set of length $L_{2D}=(2 \times F_{\max} S_N + 1) \times (2 \times F_{\max} S_M + 1) \gg L_{1D}$. As a practical example, in the two test cases reported in fig2 and fig3, $F_{\max} S_N=25$ and $F_{\max} S_M=75$, thus $L_{2D}/L_{1D, \text{TOR}}=151$ and $L_{2D}/L_{1D, \text{POL}}=51$, while the ratio of the total CPU run times is in the range $\tau_{2D}/\tau_{1D} \sim 60 \rightarrow 300$ for around $10 \rightarrow 30$ iterations of the BCD algorithm. Hence, when accounting for the initial overhead in allocating and storing the required memory, which has a different size in SS-H2 vs SS-2D, we find that for each iteration of the BCD algorithm τ_{2D}/τ_{1D} is quite similar to L_{2D}/L_{1D} .

The two test cases shown in Section-3 indicate that in some circumstances SS-2D is significantly more accurate than running twice SS-H2 (which we will call *2xSS-H2* for simplicity from now on), however a statistical analysis using simulated data, as *we know what the results must be*, is mandatory: the results of this work will be shown in the next Section. Before this statistical analysis, a number of initial tests is performed, so as to elucidate the most basic difficulties with the SparSpec-2D algorithm and to set-up fixed and optimized values for some of the multiple analysis parameters.

3a. All the probes are aligned.

If all the probes are aligned along one direction, either at $\theta=\pi$ (i.e. a purely toroidal array) or at $\phi=\pi$ (i.e. a purely poloidal array), it is very predictable that the algorithm will be unable to find the modes' components along the other direction, which becomes an ignorable coordinate. As an example, a numerical experiment can be performed by positioning all the probes at $\theta=\pi$ and creating an input signal first with a single $(m_1, n_1)=(2, 1)$ and then a single $(m_2, n_2)=(3, 2)$ component, always with amplitude $A_0=1$. For actual tokamaks, this numerical experiment corresponds to the very well-known case of low-frequency tearing modes, that must be detected correctly as their onset and un-controlled evolution can be very detrimental for the survival of the plasma discharge [30]. In these two cases, the SS-2D algorithm finds a largely dominant output component first with $(m_1, n_1)=(0, 1)$ and then with $(m_2, n_2)=(0, 2)$, respectively. Without any information on the poloidal mode structure, since θ is an ignorable coordinate in this measurement set-up, the SS-2D algorithm can only find a $m=0$ mode: as the corresponding poloidal variation of the complex mode amplitude simply becomes an additional but constant contribution to the *randomized* phase shift δ_k at each sensor, which then contributes to the detection of spurious and much lower amplitude toroidal components.

3b. All the probes are exactly in a cross-like arrangement.

Logically, putting other probes whose position vary with θ can surely help in resolving the previous problem. But if the probes are exactly in a cross-like arrangement, some artefacts appear under certain input conditions. This is for instance visible by positioning $N_{\text{SENS}}/2$ probes at $\theta=\pi$ and the other $N_{\text{SENS}}/2$ probes at $\phi=\pi$. If the signal is composed of two modes situated on a line crossing $(n,m)=(0,0)$, for instance $(n_1,m_1)=(1,2)$ and $(n_2,m_2)=(-1,-2)$, all with an amplitude $A_0=1$, the SS-2D algorithm finds these input modes but also two spurious solutions at the symmetric mode numbers $(n_3,m_3)=(1,-2)$ and $(n_4,m_4)=(-1,2)$. It is therefore very important to avoid this arrangement of sensors. Hence it appears that there is an unintended benefit coming from the minor differences between the nominal and the actual position of the sensors as installed in vessel due to the installation tolerances.

3c. The probes are positioned too closely to each other.

If all the probes are really close to each other and do not cover a sufficient portion of all the available 2D $\{\phi,\theta\}$ geometrical space, it can be expected that some modes could be rather badly reconstructed. To test this hypothesis, 40 probes are randomly positioned along the contour of a square centered at $(\phi,\theta)=(\pi,\pi)$ and with the half-length of the sides varying between $R=[0\rightarrow\pi]$. As a numerical example, the input modes of the signal are $(n_1,m_1)=(2,0)$, $(n_2,m_2)=(2,4)$ and $(n_3,m_3)=(3,-3)$, all with amplitude $A_0=1$. The overall error is then defined as $\Omega=(\sum_{n,m} A_{\text{OUT}}(n,m)-A_0(n,m))^{1/2}$, where $A_{\text{OUT}}(n,m)$ are the output mode components. Figure4 shows the main results of this analysis: the RMS and STD values of the overall error on the energy conservation, the number of iterations needed for the convergence of the BCD algorithm and the CPU run-time. It is clear that at least $R/\pi>0.4$ is needed to recover correctly the input mode spectrum in a sufficiently short computational time, and that for $R/\pi\geq 0.65$ there is not much further improvement in the accuracy and speed of the calculations.

3d. Can multiple poloidal components for the same toroidal mode number be detected?

In the typical tokamak scenario, and specifically due to the toroidal geometry, in most cases multiple poloidal components exist at the plasma edge (i.e. the plasma location closest to the position of the magnetic sensors mounted on the wall) for a single toroidal mode number. Therefore, it is important to test whether this situation can be detected correctly using the SS-2D algorithm. Figure5 shows the results of an illustrative single test run, where $N_{\text{COMP}}=3$ and $M_{\text{COMP}}=[3,2,1]$ were used, i.e. the first toroidal mode has three poloidal components, the second toroidal mode has two poloidal components, and the third toroidal mode has only one poloidal component. The results are quite satisfactory: only the lowest amplitude poloidal modes with input $A_0(m,n)<0.15$ are not detected, and essentially no spurious solutions are found.

3e. How many sensors we need in total?

As a numerical example, we consider the case of four input modes $(n_1, m_1)=(2,0)$, $(n_2, m_2)=(10,-4)$, $(n_3, m_3)=(-2,14)$, and $(n_4, m_4)=(-10,15)$, all with an amplitude $A_0=1$, thus probing the detection of low and high toroidal and poloidal mode numbers. For these test runs we use $N_{MAX}=25$, $M_{MAX}=50$, and scan $N_{SENS}=[10 \rightarrow 70]$. The results are shown in fig6: we need at least 25 sensors to recover correctly the input mode spectrum, but a much larger number >50 is counter-productive, as the (randomized in our test simulation) measurement errors start having a big impact on the accuracy of the results for too closely spaced sensors.

3f. How many toroidal and poloidal atoms we need in total?

We now check our hypothesis on the value of $\alpha_{N,M} = F_{max} S\{N,M\} / \{N,M\}_{MAX}$ by scanning $\alpha \in [1 \rightarrow 10]$ for the same input spectrum. We consider for this set of test runs five randomly chosen input toroidal modes and $M_{COMP}=[3,1,2,4,1]$, $N_{MAX}=25$, $M_{MAX}=35^8$, $N_{SENS}=40$ randomly spaced, repeating the analysis 100 times for each set of input toroidal modes. The results are plotted in fig7, where we show the RMS and STD values of the overall error on the energy conservation, the number of iterations needed for the convergence of the BCD algorithm and the CPU run-time. A rather characteristic bell-shape curve is obtained, with a minimum around $\alpha=5 \rightarrow 6$ but already for $\alpha=3$ the relative error on the energy conservation $\Delta E/E$ is close to the input $\{\sigma_k, \sigma_l\}=0.15$. It is clear that the use of the BCD algorithm can be optimized: too few atoms make the calculation faster but less accurate, while too many atoms increase the CPU run-time without improving much the performance of the algorithm. Therefore, the practical limit for the value of α (which in principle could be different for the toroidal and poloidal analyses) becomes also determined by the available RAM on the platform used for the SS-2D calculations.

3g. Performance of SS-2D vs. 2xSS-H2 as function of the (simulated) measurement errors.

Finally, we can now check the dependence of the SS-2D accuracy and speed on the measurement errors, simulated in this specific test case. We consider for this set of test runs five randomly chosen input toroidal modes with a fixed $M_{COMP}=2$ (randomized at each run) for each toroidal mode, $N_{MAX}=15$, $M_{MAX}=25$, $\alpha=5$, $N_{SENS}=40$ randomly spaced and not-orthogonal, $\lambda_{REL}=0.15$, and then scan randomly distributed $\{\sigma_k, \sigma_l\}=[0.00 \rightarrow 0.35]$. We repeat the analysis 100 times for each value of σ_k and σ_l : note that while we scan σ_k we then always keep a fixed $\sigma_l=0.05$ for simplicity of interpretation,

⁸For this test we had to use a lower value for N_{MAX} and M_{MAX} as for $\alpha>5$ we run out of available RAM for the Matlab session on the laptop where the analyses are performed when using the usual values $N_{MAX}=35$ and $M_{MAX}=50$.

and the same when scanning σ_1 . The results are plotted in fig8, where we show the RMS and STD values of the overall error on the energy conservation, the number of iterations needed for the convergence of the BCD algorithm and the CPU run-time. As expected, and consistently with all the previously reported results for SS-H2 and SS-V5, the measurement performance decreases for increasing measurement errors, but we do not really find any threshold value in $\{\sigma_k, \sigma_1\}$ above which the performance of SS-2D deteriorates excessively. Thus, we confirm our empirical and a-priori setting of a fixed maximum value for both $\{\sigma_k, \sigma_1\}=0.15$ for the ensuing analyses, essentially with the aim of reducing the overall computational costs while keeping realistic measurement errors which are in line with the typical ones for magnetic diagnostic systems in currently operating tokamaks.

5. A statistical analysis of the performance of SS-2D.

Having performed the initial set of simulations reported in Section-3a to 3g, we now need to define which of the many other input analysis parameters we would like to use so as to test the performance of SS-2D vs. 2xSS-H2, namely accuracy and required computational time.

First, it is well known from the extensive experience using SS-H2 (and also SS-V5) that setting a correct value for λ_{REL} is essential for obtaining an accurate solution. For the 1D analyses, a scaling can be found empirically (by running numerical experiments on given datasets) to determine the nominal correct value for λ_{REL} . We find that λ_{REL} must decrease linearly for an increasing number of output physical components to be obtained for a given set of input components, from $\lambda_{REL,MAX}>0.85$ for 1 output mode to $\lambda_{REL,MIN}<0.15$ for more than 5 output modes. It is then paramount to verify if a similar scaling is also valid for SS-2D, particularly finding the appropriate values for $\lambda_{REL,MAX}$ and $\lambda_{REL,MIN}$. Therefore, this is the first statistical analysis that we will perform.

Second, as it has already partially transpired from the one-off test cases presented in Section-3, the main advantage of SS-2D vs. 2xSS-H2 is when the sensors are not orthogonal. Therefore, the second statistical analysis is performed comparing orthogonal vs. non-orthogonal arrangements of sensors. For this set of tests, we always use sensors which have a random poloidal distribution, but also allow for an equi-spaced toroidal distribution. This choice comes from the arrangements in existing devices: poloidal sensors can essentially never be uniformly distributed, simply because their actual position with respect to the last closed flux surface (LCFS) is equilibrium-dependent (the so-called *thetastar* correction [31,32]), and thus this can never be always the same. Conversely, it is a common practice to attach toroidal sensors to the in-vessel poloidal rails joining the toroidal sectors of the machine, hence an equi-spaced arrangement can always be obtained first, which can then be altered by adding

additional and non-uniformly spaced sensors at some specific locations in-between these rails (as an example, see the ITER case, fig1c).

Third, the very different accuracy and CPU run-time needed by SS-2D vs. 2xSS-H2 observed in the single test runs shown in Section-3 need to be checked more systematically against the number of input component, specifically with respect to the ratio M_{COMP}/N_{COMP} at a fixed value of N_{COMP} .

To summarize, in our statistical analyses reported in this Section we will always use:

- $N_{SENS}=40$ sensors, $N_{MAX}=35$ and $M_{MAX}=50$, $\max(\{\sigma_k, \sigma_l\})=0.15$ (in relative units), $\{\delta_k\} \in 0.2 \times \pi$, $\alpha_{N,M}=[3,3]$, $n_{IT}=1000$ and $TR_{IT}=1 \times 10^{-5}$;
- scan-1, see Section-4a: for $N_{COMP}=1 \rightarrow 10$ and at fixed $M_{COMP}=N_{COMP}$, we analyse the same input spectrum as acquired by non-orthogonal sensors, scanning $\lambda_{REL} \in [0.05 \rightarrow 0.95]$ for each value of N_{COMP} ; this allows to determine the optimal value of $\lambda_{REL}(N_{COMP})$ to be used in the next scans.
- scan-2, see Section-4b: for $N_{COMP}=1 \rightarrow 5$ and at fixed $M_{COMP}=N_{COMP}$, we analyse the same input spectrum as acquired by orthogonal vs. non-orthogonal sensors, always using the previously determined value of $\lambda_{REL}(N_{COMP})$.
- scan-3, see Section-4c: for $N_{COMP}=1 \rightarrow 5$ and varying $M_{COMP}=[1 \rightarrow 5] \times N_{COMP}$, we analyse the same input spectrum as acquired by non-orthogonal sensors, always using the previously determined value of $\lambda_{REL}(N_{COMP} \times M_{COMP})$, extrapolating if needed from the results of the first scan.

For each scan, a very large number of simulations $N_{ITER}=10'000$ will always be run to avoid possible bias in the analyses, which could be due to the different (and possibly randomized) sensors' geometry and input spectrum used in each individual run. Conversely, when comparing orthogonal vs. non-orthogonal sensors, the same input spectrum is used. Globally, we will compare the RMS and STD values of the total relative error on the input vs. output energy conservation ($=\Delta E/E$), the number of faults in correctly finding the input components, the number of iterations needed for the convergence of the BCD algorithm ($=n_{ITout}$) and the CPU run-time ($=\tau_{CPU}$), comparing the results of SS-2D vs. those of 2xSS-H2. Note that the number of faults is normalized with respect to the length L of the physical mode base, different for the 2D analysis, $L_{2D}=(2 \times N_{MAX}+1) \times (2 \times M_{MAX}+1)$ and the separate 1D toroidal and poloidal analyses, respectively $L_{1D,TOR}=(2 \times N_{MAX}+1)$ and $L_{1D,POL}=(2 \times M_{MAX}+1)$. This accounts for the fact that it is more likely to find spurious output components within a much larger set of physical atoms.

4a. Comparison between SS-2D vs. 2xSS-H2: varying λ_{REL} .

For this scan we vary $\lambda_{REL}=[0.05:0.15:0.95]$ and use $N_{COMP}=1 \rightarrow 10$ at fixed $M_{COMP}=N_{COMP}$: the results are reported in fig9a for randomly spaced toroidal sensors, and in fig9b for equi-spaced toroidal

sensors, respectively. The number of faults is typically 6x lower for SS-2D than for 2xSS-H2, a clear improvement in the performance. The results are however more complex to interpret for the energy conservation: we find that for a sufficiently low number of components, up to $N_{\text{COMP}}=3$, SS-2D clearly out-performs 2xSS-H2 for all values of λ_{REL} ; however, for $N_{\text{COMP}}>5$ the SS-2D results are much less convincing, particularly for a higher set value for λ_{REL} . Note in any case the significantly larger CPU run-time requirements for SS-2D: typically τ_{CPU} is 260x (for randomly spaced toroidal sensors) to 320x (for equi-spaced toroidal sensors) longer for SS-2D than for 2xSS-H2, due to a significantly larger value of $n\text{ITout}$.

4b. Comparison between SS-2D vs. 2xSS-H2: orthogonal vs. non-orthogonal sensors.

Using the results of the λ_{REL} -scan shown in Section-4a, we now set a fixed value $\lambda_{\text{REL}}=0.15$ and compare the results of SS-2D vs. 2xSS-H2 when using orthogonal vs. non-orthogonal sensors. The results of this analysis are shown in fig10: we now find a clear improvement from SS-2D when using an optimal value for λ_{REL} and up to $N_{\text{COMP}}=5$ toroidal and poloidal components, specifically when non-orthogonal sensors are used. The computational cost is however very high: τ_{CPU} is typically $\sim 330x$ times longer for SS-2D than for 2xSS-H2, again due to a significantly larger value of $n\text{ITout}$. As shown in fig11 for comparison purpose, using an even smaller $\lambda_{\text{REL}}=0.05$ does not bring about any significant improvement in the performance of SS-2D, and therefore for all further analyses we now keep only the optimized value $\lambda_{\text{REL}}=0.15$.

4c. Comparison between SS-2D vs. 2xSS-H2: varying $M_{\text{COMP}}/N_{\text{COMP}}$.

Next, we test the accuracy and the computational cost of SS-2D vs. 2xSS-H2 as function of the number of poloidal components for each toroidal mode, using only randomly distributed and non-orthogonal sensors. The results of these analyses are shown in fig12, and it is very clear that SS-2D definitively out-performs 2xSS-H2 in terms of accuracy when multiple poloidal components exist for a single toroidal mode, which is the typical experimental situation in tokamaks. Due to limitations in the available RAM in the laptop used for these simulations, only a fixed $\alpha=3$ could be used, and this is likely to become sub-optimal when $N_{\text{COMP}} \times M_{\text{COMP}} > 10$. Also note that the initial value of $\lambda_{\text{REL}}=0.15$ is only valid up to $N_{\text{COMP}} \times M_{\text{COMP}}=10$: for a larger value of components we then further reduce it linearly towards $\lambda_{\text{REL}}=0.05$ at the maximum value $N_{\text{COMP}} \times M_{\text{COMP}}=25$. Both these numerical settings are likely to be sub-optimal and this explains the clear deterioration of the performance of SS-2D for $N_{\text{COMP}} \times M_{\text{COMP}} > 12$.

4d. Summary of the results of the statistical analyses.

Summarising the results obtained in Section-4a to 4c, it appears that:

1. SS-2D is accurate and thus useful essentially for a low number of input components, at the most up to $N_{\text{COMP}} \times M_{\text{COMP}} = 10 \div 12$, practically irrespectively of the arrangement of toroidal sensors, i.e. be these randomly or uniformly distributed;
2. a rather low value of $\lambda_{\text{REL}} \leq 0.15$ need to be set for SS-2D even for such a relatively low number of input components, which is lower than that needed for the 1D analyses using SS-H2;
3. the best arrangement of toroidal vs. poloidal sensors for use by SS-2D is the non-orthogonal installation setup;
4. finally, the computational cost of SS-2D is very high, typically $\sim 300x$ longer than that required by 2xSS-H2, and also the RAM consumption becomes prohibitive when a very large dictionary of atoms needs to be used.

6. An actual test case from the JET tokamak.

We now consider an actual test case from the JET tokamak, using the 8x high resolution toroidal and poloidal H30N sensors, whose position is shown in fig1b. This set of HF magnetic sensors has had quite a troubled history in JET [33], and the last time most of them have been working correctly is the early 2000, unfortunately, when only H308 was not operational. Therefore, for this test case we consider the rather old JET shots #49384 and #55604, which were used to identify the occurrence of Alfvén Cascades (ACs) in plasmas with a non-monotonic profile for the safety factor [34].

In #49384 only Ion Cyclotron Resonance Frequency (ICRF) heating was used during the ohmic current ramp-up phase, thus the safety factor (q -) profile was monotonic with $q_0 < 1$ in the plasma core, and the usual fast ion driven Toroidal Alfvén Eigenmodes (TAEs) were found at frequencies in the TAE gap, see fig13a, namely between 80kHz and 150kHz during the current ramp-up phase. Note that $df_{\text{TAE}}/dt \propto B/\sqrt{n_{e0}/q_{\text{RES}}}$, where $\{B, n_{e0}\}$ are the toroidal magnetic field and the central electron density, respectively, while $q_{\text{RES}} = (2m_{\text{TAE}} + 1)/2n_{\text{TAE}}$ is the value of the safety factor at the mode resonant position, where m_{TAE} and n_{TAE} are the toroidal and poloidal mode number of this mode, respectively. Therefore, at sufficiently constant plasma density and fixed toroidal magnetic field $df_{\text{TAE}}/dt \propto I_p$, where I_p is the (purely ohmic in this case) plasma current, thus the TAE mode frequency essentially increases linearly during the initial (ohmic) current ramp-up phase. Theoretical modelling indicates that TAEs have typically multiple poloidal harmonics for a given single toroidal mode number, such that the m_{POL} measured by magnetic sensors can reach values up to $m_{\text{TAE}} \times q_{\text{LCFS}}$, where q_{LCFS} is the value of the safety factor at the LCFS.

In #55604 Lower Hybrid Current Drive (LHCD) was applied together with ICRF early and this increased the plasma conductivity off-axis through direct heating of the electrons, which then prevented the ohmic current from penetrating to the plasma core, in turn producing a non-monotonic safety factor profile, with the minimum value q_{MIN} towards mid-radius and $q_0 > 1$. In #55604 we thus observed modes with a characteristically slow upward frequency sweep, see fig13b, for which df_{TAE}/dt is not directly correlated with I_p . The highest frequency of these modes was just reaching the bottom of the TAE gap at around 100kHz, with a characteristic hockey-stick pattern at these frequencies. Therefore, these modes could not be TAEs: theoretically modelling [34, 35, 36] demonstrated that these are still modes driven by energetic particles (EPMs) whose upward frequency sweep tracks the evolution of the minimum in the safety factor profile $q_{\text{MIN}}(t)$. These EPMs are often called Alfvén Cascades and/or Reverse Shear Alfvén Eigenmodes and a necessary condition for their existence is that the pair of toroidal and poloidal mode numbers n_{AC} and m_{AC} can only appear at the time $t=t_0$ if $m_{\text{AC}} - n_{\text{AC}} \times q_{\text{MIN}}(t) = 0$, i.e. (a) $q_{\text{MIN}}(t_0)$ must pass through the relevant rational value $m_{\text{AC}}/n_{\text{AC}}$, and (b) only one single poloidal component exist for a single toroidal mode. Note that the temporal derivative of the AC mode frequency is proportional to the toroidal mode number, $df_{\text{AC}}/dt \propto n_{\text{AC}}$ at fixed plasma density and magnetic field.

It is therefore very interesting to test whether these results can be found using SS-2D for a concurrent toroidal and poloidal mode number analysis: fig13(a,b) shows the spectrograms (i.e. the analysis was performed on the Fourier Transform of the input time series) for the measured poloidal mode numbers ($=m_{\text{MEAS}}$) for these two discharges. These spectrograms were produced at the time of the experiment and show m_{MEAS} as calculated using the only analysis method available at the time, namely the classical linear phase fit method: $\Theta_{\text{POL}} = c_0 + m_{\text{MEAS}} \times \theta$. Here Θ_{POL} is the phase of the signal at the specific time ($=t_0$) and frequency (f_0) in the spectrogram, and c_0 is an arbitrary constant. With this method, $m_{\text{MEAS}} = \Sigma(m \times A_{\text{POL}}^2) / \Sigma A_{\text{POL}}^2 \notin \mathbb{N}$, i.e. it is a weighted sum over all poloidal harmonics and thus is generally NOT an integer. Table1 and Table2 show a summary of the data for the toroidal and poloidal mode numbers from the linear phase fit method and from 2xSS-H2 and SS-2D, as computed today, for #49284 and #55604 respectively. The SparSpec analyses were performed using $N_{\text{MAX}}=10$, $M_{\text{MAX}}=60 \sim q_{\text{LCFS}} \times N_{\text{MAX}}$, $\alpha_{N,M}=[3,3]$, $\lambda_{\text{REL}}=0.15$, $n_{\text{IT}}=1000$ and $\text{TR}_{\text{IT}}=1 \times 10^{-5}$. The spectrograms are also annotated with some of the SS-2D data.

For the TAEs in #49384 (fig13a) we find that multiple poloidal harmonics exist for each one of the toroidal mode numbers $n_{\text{TAE}}=3 \rightarrow 5$ for the measured modes. Conversely, for the ACs in #55604 (fig13b) we essentially find one largely dominant poloidal mode number. These results are clearly consistent with our theoretical understanding of these modes; however they cannot be further verified as internal fluctuation measurements that could help in identifying the modes' resonant position, and

thus confirm the value of m from that of n and $\{q_{\text{RES}}, q_{\text{MIN}}\}$, were not available for these discharges. Essentially as a numerical test, the analyses were repeated using the currently surviving set of H30N magnetic sensors, which includes only the four sensors [H302, H303, H304, H305]. In this case the toroidal mode number can still be detected correctly, but the poloidal mode number cannot. Finally, the computational costs for the SS-2D analyses are onerous, typically $\sim 300\text{msec}$ for each individual pair of time and frequency points $\{t_0, f_0\}$ in the spectrogram.

Note that the H30N sensors cover a small range in $\{\phi, \theta\}$ spanning 36deg toroidally over 5 sensors and $\sim 30\text{deg}$ poloidally over 4 sensors. A question springs immediately to mind: why SS-2D does so well even with such a reduced set of sensors and spatial coverage, which seems contrary to most of our previous simulation results? The reason is essentially that at any $\{t_0, f_0\}$ these modes have only one toroidal mode number and either one or multiple poloidal mode numbers with intermediate and close-by values. In this case (a) the corresponding total phase shift on the FT signal is detectable by and recognisable with the H30N sensors, and (b) the poloidal mode amplitude does not show any ballooning effect since the D-shaped JET wall is conformal to the LCFS and the H30N sensors cover a rather small span in poloidal angle. Conversely, the accuracy of the SS-2D results would NOT have been the same had we been looking at (a) multiple and very different mode numbers in a time series (i.e., not on the FT of the signal), which is the case for our simulations, see also the results for one of the ITER test cases, shown in Section-7, and (b) cases where the ballooning effect on the poloidal mode amplitude is very important in the FT spectrum, which is NOT considered in our simulations, see also the results for the TCV test cases, shown in Section-6.

Looking now in details at the results shown in Table1 and Table2, the estimated error on the toroidal and poloidal mode numbers calculated using the Linear Phase Fit (LPF) method ($=\{n, m\}_{\text{LPF}}$) is linked to the propagation of errors on the reconstructed fit of the mode phase; for the corresponding values $\{n, m\}_{\text{H2}}$ and $\{n, m\}_{\text{2D}}$ we also provide the mode amplitude ($=A$) for all components above the estimated S/N ratio ~ 0.10 , in normalized units such that the input vs. output energy $\propto \Sigma A^2$ is conserved in the Parseval sense. For these two JET discharges, we find that the 2xSS-H2 analyses already allow to recognise the multiple poloidal components of TAEs vs. the essentially single poloidal component for the ACs. We cannot find any clear advantage in using SS-2D vs 2xSS-H2 for these analyses using the H30N sensors, particularly those currently surviving.

It remains to be seen, however, and this is beyond the scope of this work, whether for current analyses SS-2D becomes more useful in terms of accuracy, even if at a much higher computational cost, than 2xSS-H2 when adding all, or most of, the other toroidal and poloidal sensors to the surviving set of H30N sensors. Currently, it is unclear whether the different arrays of JET magnetic sensors can be efficiently combined as they are characterized by a very different frequency-dependent transfer

function, and thus are likely to have very different intrinsic, frequency-dependent measurement errors. Precisely this problem has prompted the development of the different versions of the SS-V5 algorithm [1,2] for the 1D analyses, and our next step is exactly that of extending SS-V5 to the 2D analyses, specifically SS-V5b0 to track correctly the propagation of errors on the analysis results.

7. An actual test case from the TCV tokamak.

We can now consider an actual test case from the TCV tokamak, and for this analysis we consider #70281, a shot with Neutral Beam Injection (NBI) which provides the source of fast ions driving the so-called sawbones [37,38], i.e. the variant of the well-known fishbones [39] that occurs with quasi-tangential NBI and inevitably causes a sawtooth crash. Figure14 shows the time trace for one of the magnetic signals on the LFS and HFS midplane over the time window of interest, together with the main background plasma parameters. This data, particularly for the electron density and temperature, are plotted on the coarse time resolution of the equilibrium reconstruction, which does not allow to see the characteristic sudden crash associated to each individual sawtooth.

The sawbones are well-known to be $m=1/n=1$ modes, however the fully processed magnetic traces at the frequency of interest give a value for the poloidal mode number $m_{MEAS} \sim q_{LCFS}$, i.e. close to the value of the safety factor at the LCFS. This *surprising* result can be understood by calculating the poloidal structure of the mode using the KINX code [40]. Figure15 shows the results obtained at $t=0.6208\text{sec}$, i.e. the closest equilibrium time point to that of the onset of the sawbone at $t=0.6213\text{sec}$. It is very evident from these analyses that indeed the sawbone is a $m_{RES}=1/n=1$ mode at its corresponding resonant q -surface, however due to the Alfvén law of flux conservation and overall conservation of the mode's helicity⁹ the poloidal mode structure at the LCFS shows all poloidal harmonics up to $m=n \times \text{fix}(q_{LCFS})$, i.e. the closest integer (from below) to q_{LCFS} . The harmonics-weighted value of m_{KINX} from KINX is ~ 2.8 at the LCFS, quite close to the measured value $m_{MEAS} \sim 3.3 \pm 0.1$ estimated using a linear phase fit of the Fourier Transform of the poloidal signals for the sensors on the LFS (more on this later ...). In general, m_{MEAS} estimated with this approach is quite close to the ansatz $m_{MEAS} \sim m_{RES} \times q_{LCFS} / q_{RES}$ for TCV plasmas.

The FT of the processed magnetic signals shows that the sawbone has multiple harmonics, and for these analyses we just focus on the fundamental, namely the one calculated with KINX: the data are

⁹Empirically, if an internal mode, i.e. resonant at a q -surface rather far away from the LCFS, does not have the same helicity as that of the background plasma, it is heavily stabilized by the magnetic shear, therefore due to toroidicity effects across the poloidal cross-section additional poloidal harmonics must have appeared if the mode has been picked-up by magnetic sensors at the wall. Therefore, m_{MEAS} depends on where the measurement is made, while n is the same across the poloidal cross-section for axisymmetric plasmas, and locally the dominant poloidal harmonics are such that $m_{MEAS}/n_{RES} \sim q(\rho)$, i.e. the mode helicity is conserved.

shown in fig16 for the toroidal and poloidal decomposition, respectively. The magnetic measurements are compared at four poloidal sectors separated by $\pi/2$ and for six toroidal arrays located on the LFS and HFS at $Z=0$ (the *MID* array), $Z=+345\text{mm}$ (the *TOP* array) and $Z=-345\text{mm}$ (the *BOT* array). Since the plasmas sits at $Z_{\text{MAG}} \sim 30\text{mm}$ and has positive triangularity, the toroidal {LFS, HFS}-{MID, TOP} arrays provide the more sensitive measurements. The difference between the corresponding sets of data on the LFS vs. the HFS indicates the possible ballooning structure of the mode, i.e. the role of the pressure gradient vs. the curvature of the magnetic field for the mode stability.

Due to toroidal axisymmetry, we expect the measurements from the four poloidal arrays to be very similar, which is the case; however, the variation of the poloidal mode amplitude $A(\theta^*)$ over the poloidal angle θ^* in the field-aligned (thetastar) coordinate system at the LCFS is problematic for the analysis. In fact, the main assumption of the SparSpec algorithm is that the variation of the signal over the angular coordinate is solely due to a dependence on the mode number: for the poloidal analyses, this means $A_m(\theta^*) = A_{0,m} \times \cos(m\theta^*)$. Conversely, in the TCV case the measured poloidal variation is also due to the different distance ($=d_w$, calculated along the normal to the LCFS) between the LCFS and the magnetic sensors at the wall, thus $A_m(\theta^*) = A_{0,m}(d_w(\theta^*), \theta^*) \times \cos(m\theta^*)$. Hence, we always only use the liner phase fit method to determine the apparent m_{MEAS} , and then considering only the poloidal sensors on the LFS (namely, the sensors 16 to 24 as shown in fig1a, for a total of 9) due to the possible ballooning structure of the mode. Such a procedure, however, does not allow to determine if the poloidal mode structure has multiple components, and this is precisely why we now attempt to use SparSpec-2D after a renormalization of the poloidal mode amplitude as function of d_w . For this, we assume a WKB model for the decay of the wavefield in the vacuum region between the LCFS and the wall: $A_{\text{WALL}} = A_{\text{LCFS}} \times \exp(-k_{\perp} d_w)$. Here k_{\perp} is the perpendicular wavenumber in this region and for it we take the proxy $k_{\perp} = 2\pi \times (|m_{\text{MEAS}}| + 1) / L_{\text{MAG}}$, where L_{MAG} is the magnetic field connection length, so that A_{WALL} and A_{LCFS} are the mode amplitudes at the wall (namely, that directly measured by the magnetic sensors) and reconstructed at the LCFS, respectively.

For the SS-2D analyses, and for testing purposes, we combine the data from the LFS-MID array, which has two sensors (out of a total of 17) slightly displaced poloidally, or from the LFS-TOP array, for which all the sensors are exactly at the same poloidal position, with all LFS poloidal sensors in any of the four toroidal sectors fully equipped. For illustrative and consistency purposes, we consider all 28 sawbones that appear in #70281 before the large crash at $t=0.87\text{sec}$, thus intrinsically assuming that the same physics applies for understanding the results from the KINX code. The FT data are computed over the time window centred at the time of the sawbone crash $\pm 128\mu\text{sec}$ (the acquisition frequency is 500kHz, so the FT time window encompasses a power-of-2 number of time points, which improves the FT accuracy as it avoids zero-padding).

Figure 17(a,b) show the results of the detailed analyses performed with SS-2D vs. those performed with SS-H2 for the sawbone at $t=0.6213\text{sec}$, using the data from the LFS-MID and the POL-011 arrays. The SparSpec analyses are performed using $N_{\text{MAX}}=6$, $M_{\text{MAX}}=15$, $\alpha_{N,M}=[3,3]$, $\lambda_{\text{REL}}=0.15$, $n_{\text{IT}}=1000$, $\text{TR}_{\text{IT}}=1\times 10^{-5}$. Comparing the experimental results with the modelling from KINX, we find that indeed SS-2D can resolve the multiple poloidal components of the mode, while SS-H2 clearly misses some components and allows spurious ones. The greater accuracy provided by SS-2D comes however with a significantly higher computational cost, around 65msec compared to less than 1msec for the SS-H2 analyses. Note that the excellent results by SparSpec-{1D,2D} for the poloidal decomposition are clearly conditional on having modelled correctly the decay of the mode amplitude as function of the distance from the LCFS. It is then reasonable to ask ourselves if applying SparSpec to TCV analyses is actually worth the effort, due to the quasi-orthogonal positioning of the sensors, with one ignorable coordinate for most, if not all, of them. The toroidal sensors are essentially equi-spaced, hence a standard Fourier decomposition already works very well, and an ad-hoc functional is absolutely needed to (at least partially) compensate for the ballooning structure of the modes, while a linear phase fit already works well for the poloidal analyses, even if it does not allow to distinguish between different components. The ITER test analyses reported in Section-7 will show that there are indeed useful applications of SS-2D, but not really for TCV analyses.

8. A set of simulated test cases for the ITER tokamak.

While the TCV test case has demonstrated that SS-2D does not bring about much advantage, we now look at the ITER tokamak to check whether for a more generic arrangement of sensors SS-2D brings about any benefits. This is precisely the case of ITER for the two groups of sensors highlighted in green in fig1c, which are very closely spaced (as the H30N sensors in JET), but for which one coordinate is not ignorable. Our analyses use the algorithm for signal generation developed in [29], comparing the results obtained with the sensors highlighted in *red* and *blue* in fig1c, used by SS-H2, with those highlighted in *green*, used by SS-2D.

The ITER measurement specifications [41, 42] demand that modes up to $|n|=20$ be correctly detected, i.e. within a ± 0.5 accuracy, and that the corresponding poloidal mode numbers are also correctly detected, within a ± 0.5 accuracy, without however specifying a measurement range: we then assume that this has to apply up to $|m|=30$. The subset of equi-spaced toroidal *red* sensors at the same vertical position (for instance extracted from those sitting around $\theta_{\text{GEOM}}=30\text{deg}$, i.e. the top toroidal *red* array in fig1c) only allows detecting $|n|\leq 9$ as they are exactly equi-spaced by $\pi/18$. Adding (some of) the *red* sensors at a different vertical position allows to remove the Nyquist limitation, at the expense however of introducing errors through the dependence on the poloidal mode numbers. Similarly, for

the poloidal analyses the *blue* sensors are not all at the same toroidal angle, and this introduces errors particularly for high toroidal mode numbers, and correspondingly high poloidal mode numbers. Thus, there is a clear potential for concurrent 2D toroidal and poloidal analyses, and the two groups of *green* sensors are particularly suited for this task.

The potential for a concurrent 2D analysis in ITER is also linked to the intended long-term (~30 years) operation of these in-vessel magnetic sensors without maintenance nor replacement. It is inevitable that some of these sensors will fail due to irradiation and neutronics damage, and thus to maintain the same measurement performance it is correspondingly inevitable that sets of sensors without one ignorable coordinate will have to be used at some point during the life-time of ITER.

Following from the description presented in [29], we construct a set of time traces for the measured voltage $V_{\text{MEAS},k}(t) = N A_{\text{EFF},k} \times dB(t)/dt + \sigma_k(s)$ for all the *red* and *green* sensors, hence simulating the measurements at the sensors' position. Here $N A_{\text{EFF},k}$ and $\sigma_k(s)$ are the effective area and the intrinsic measurement error in the Laplace domain, for each sensor. For these analyses the analogue vs. digital transfer functions are not used, as their role is not directly linked to the use of SparSpec. ITER plasmas are foreseen to have a LCFS essentially conformal to the wall, thus $\exp(-k_{\perp}dw)$ is the same for all sensor, therefore there is no need to rescale the mode amplitudes as for the TCV analyses, which greatly simplifies the overall understanding. Each time trace includes the same modes (=Eigenmodes) at various frequencies and with different toroidal and poloidal mode numbers, and each mode has a time-varying frequency and amplitude. This signal is then *polluted* with a background continuum component following a power-law spectrum and random (thus individualized for each sensor) noise with a characteristic colour. We then perform a Power Spectral Density (PSD) and an ensuing Fast Fourier Transform (FFT) analysis, dubbed PSD+FFT for simplicity, on each time trace and then apply SS-H2 and SS-2D, evaluating the overall *score* of the simulation results. As explained in details in [29], such score $\in [0 \rightarrow 1]$ accounts for the accuracy of the analysis in recovering the known input modes, namely their frequency¹⁰, amplitude and toroidal and poloidal mode numbers. Our simulations consider the case where at any frequency there is only one toroidal component, and single or multiple poloidal components depending on the physics of that Eigenmode. For illustrative purposes, fig18 shows the time trace and the frequency spectrum for one simulation and for one of the sensors considered in our analyses.

Each simulation is run *only* 100 times for statistical purposes, as it takes ~6hr of CPU time to generate the input signal over the entire set of *red*, *blue* and *green* sensors over a time window of ~35msec at

¹⁰Since the analogue vs. digital calibration is not considered here, and the Eigenmodes have all a large amplitude with respect to the continuum background spectrum, the mode frequency is always found essentially exactly, i.e. the output mode frequency and its half-width at half-prominence (HWP) from the PSD analysis always contains the input value.

a sampling frequency =2MHz, and then perform the analysis of the toroidal and poloidal mode numbers with the different algorithms considered here. Thirty-two individual time windows of 1.024msec each can be analysed for each simulation (the edges of the simulation are always removed to avoid numerical problems with the integration (and the possible calibration) of the input signal). The 100x runs for each simulation are generated by randomizing the colour and intensity of the noise, set to be in the range $\max(\sigma_k)=0.15$, the power-law scaling for the continuum background spectrum around the Kolmogorov value $\alpha=-5/3$, namely from $\alpha=-4/3$ to $\alpha=-6/3$, and the relative amplitude of the different poloidal components, always using a single mode frequency with a unique toroidal mode number and keeping fixed the number of poloidal components. Multiple Eigenmodes are used for each simulation, with well-separated frequencies to avoid errors not specifically linked to the use of SparSpec. For the statistical SparSpec analyses reported in this Section, we have always used $N_{MAX}=20$ and $M_{MAX}=30$ as per the ITER measurement specifications, $\alpha_{N,M}=[3,3]$, $\lambda_{REL}=0.15$, $n_{IT}=1000$, $TR_{IT}=1 \times 10^{-5}$.

For the toroidal-1D analyses, we use the full set of *red* sensors at $\theta_{GEOM} \sim \pm 30 \text{deg}$ and we compare the results from the LPF method with those obtained with SS-H2, where we obtain the harmonic-averaged toroidal mode number $\langle n_{OUTH2} \rangle = \sum_k n_k A_k^2 / \sum_k A_k^2$, k being the index of all non-zero modes found with SS-H2 (we also constrain for simplicity and consistency $\sum_k A_k^2 = 1$). Therefore, $\langle n_{OUTH2} \rangle$ can then easily be checked against n_{OUTLF} . For the poloidal-1D analyses, we use the two sets of *blue* sensors, and we compare m_{OUTLF} with the similarly constructed harmonic-averaged poloidal mode number $\langle m_{OUTH2} \rangle = \sum_k m_k A_k^2 / \sum_k A_k^2$. For the {toroidal + poloidal} 2D analyses we use both sets of green sensors and again we obtain the harmonic-averaged value of the toroidal and poloidal mode numbers. Finally, we also consider the overall score of the simulation and the CPU run-time, noting however that the CPU run-time for SS-2D includes the concurrent {toroidal + poloidal} analyses, therefore it cannot be directly compared with the CPU run-time for the LPF and SS-H2 analyses, which includes only the toroidal and/or the poloidal analyses separately.

Further to the description given in [29], the simulation score is computed as follows, separately for the toroidal and poloidal analyses¹¹. The score is set to be =1.00 for perfect detection, and is penalized for each Eigenmode accordingly to the joint probability function of obtaining the output results, with their intrinsic scatter over the 100x simulations, within the input values with their intrinsic expected measurement accuracy σ_{IN} . For SparSpec, the score is further penalized proportionally to the number of *missed* components, i.e. input components that are NOT found in the output. Note that it is not

¹¹As it will transpire later, the high toroidal mode numbers are typically AEs, which have multiple poloidal components, with successive and high poloidal mode numbers with similar amplitudes, a situation where it is essentially impossible to exactly determine each component. Thus, an overall score for the combined {toroidal + poloidal} analyses would indeed be heavily penalized by the latter, completely masking the fact that the former could be essentially correct ...

possible to do the same for the LPF method, which is thus always favorably (and unfairly, in a sense) compared to the SparSpec methods. Since multiple poloidal mode numbers are accepted as input, and their amplitude can be chosen to be randomized, then $\langle m_{IN} \rangle$ is also defined as the average value of m over all the 100x simulations run for each toroidal mode.

$$\boxed{\begin{aligned} score(y_{IN}) = & \int_{-\infty}^{+\infty} dx \frac{1}{\sqrt{2\pi}\sigma_{IN}} \exp\left[-\frac{(x - y_{IN})^2}{2\sigma_{IN}^2}\right] \times \\ & \int_{-\infty}^{+\infty} dx \frac{1}{\sqrt{2\pi}\sigma_{OUT}} \exp\left[-\frac{(x - y_{OUT})^2}{2\sigma_{OUT}^2}\right] + \text{penalty}(\text{missedModes}) \end{aligned}} \quad (6)$$

Considering now as a practical example the case of correctly detecting the variable $y_{IN \pm \sigma_{IN}}$, with $y_{OUT \pm \sigma_{OUT}}$ being the corresponding output value, the score is then simply given by eq.(6). Note that σ_{IN} is array-dependent (due to the number and positioning of the sensors) and also, most importantly, method-dependent, as the LPF method uses only the phase of the magnetic signals, while the SparSpec methods also use the amplitude of the magnetic signals. Thus, and perhaps counter-intuitively, the intrinsic measurement accuracy for mode number detection using the SparSpec methods is always slightly larger than that for the LPF analyses.

The values for σ_{IN} are in principle frequency-dependent and are generated by polluting the exact complex {amplitude, phase} FT signals for each mode number with a randomly generated error signal accounting for all frequency-dependent measurement uncertainties for all the sensors belonging to the selected array. These *equivalent FT measurements* are then analysed with the selected method and this procedure is repeated 1'000 times for statistics. Figure19 shows the expected uncertainties for the toroidal and poloidal mode numbers used in the simulated ITER cases considered here, where we use the frequency-independent nominal values $\{\max(\sigma_k)=0.15, 10\text{deg}\}$ for the amplitude and phase measurement uncertainties, respectively. The SS-2D method out-performs the 1D methods for higher toroidal mode numbers: for the selected groups of sensors there is not an ignorable coordinate, thus the phase differences along the coordinate orthogonal to the intended measurement can only be correctly dealt with by a 2D method.

The simulations are performed using a first set of test cases with only low- n /low- m modes, $n=1/m=1$, $n=1/m=2$ and $n=3/m=5$, which correspond to TMs with a single dominant poloidal component at the resonant q -surface. Assuming a value of $q_{LCFS}=5$ and the ansatz $\max(m_{LCFS}) \sim m_{RES} \times q_{LCFS}/q_{RES}$, a second set of test cases is generated keeping the same low- n modes but now using multiple poloidal components with fixed or randomized amplitudes, i.e. considering the effect of toroidicity as for the TCV sawbones. Next, we consider TAEs with $n=\{5,8,12,15,20\}$, i.e. up to the maximum value given by the ITER measurement specifications. These modes have two dominant poloidal harmonics $\{m_{RES}$,

$m_{\text{RES}}+1$) at the resonant q-surface $q_{\text{RES}}=(2m_{\text{RES}}+1)/2n$. The third set of test cases considers only these two poloidal components for the TAEs, while the fourth (and last) set considers the toroidicity effects to get multiple poloidal components up to $\max(m_{\text{LCFS}})$, again with fixed or randomized amplitudes.

Figure 20 shows the results of these analyses, and the exact correspondence between simulation # and test case is reported in Table 3. The toroidal mode numbers are generally correctly determined for all methods and all sensors' arrangements (see the bottom subplot), namely the absolute difference $\text{rms}(|n_{\text{TOROUT}}-n_{\text{TORIN}}|)<0.2$ most often, but the scatter is significantly larger for the 1D methods when applied to sensors' arrangements without an ignorable coordinate for higher n_{TORIN} and/or when multiple poloidal components are present in the input signal. Essentially the same result is obtained for the poloidal mode numbers (see the 2nd subplot from the bottom of the figure), but now the poloidal components can be badly reconstructed (a very large scatter) even for low- n_{TORIN} modes when there are multiple poloidal harmonics. The CPU run-time for SS-2D is essentially the same for all simulations (see the middle subplot), while it rapidly increases for 2xSS-H2 for higher toroidal modes with multiple poloidal components. However, around 500msec are needed for each calculation (namely: for each mode frequency in each time interval) with SS-2D, and in absolute terms this is simply too much, and thus unattractive for routine analyses, even off-line. Regarding the simulation score for the toroidal analyses (see the second subplot from the top), this remains sufficiently high in all cases, as it is to be expected: we note however the increasing scatter for higher n_{TORIN} and when multiple poloidal components are present. Regarding the simulation score for the poloidal analyses (see the top subplot), this clearly drops for higher n_{TORIN} and, consequently, higher (and multiple) poloidal components. We note however that for the intermediate n_{TORIN} that are most interesting for ITER, SS-2D consistently out-performs 2xSS-H2, due to a higher score with a smaller scatter around its rms value.

In summary, we find that the SS-2D method clearly out-performs 2xSS-H2 (for the separate toroidal and poloidal analyses) in terms of accuracy for higher toroidal mode numbers, and as soon as there are multiple poloidal components with comparable amplitudes: the overall simulation score is higher and the scatter on the detected mode number is lower. This is simply due to having had to use arrays which cannot have any more an ignorable coordinate if the Nyquist limitation (toroidal analysis) and high-mode number detection with sufficiently good accuracy (the ITER measurement specifications for toroidal and poloidal analyses) have to be overcome. The computational cost of SS-2D vs. 2xSS-H2 is however typically at least 10x higher.

9. Summary, conclusions and an outlook to future work.

Up to this work, the main limitation of the SparSpec algorithm, in all its variants, was that it could be deployed only for 1D analyses, and most preferably using arrays with a (quasi-)exactly ignorable coordinate. Here we have extended the baseline version of SparSpec-1D, known as SS-H2, to allow for a concurrent 2D spatial analysis, comparing results from purely numerical simulations and multiple test cases from TCV and JET (real data) and ITER (simulated data but based on a clear and adequate physical model).

For arrays which do not have a (quasi-)exactly ignorable coordinate, we find that SS-2D out-performs 2xSS-H2 in terms of detection accuracy essentially for higher toroidal mode numbers, and as soon as there are multiple poloidal components with comparable amplitudes. This is indeed the general case of the ITER HF magnetic diagnostic system if the measurement requirements for toroidal and poloidal mode number analyses have to be satisfied. For ITER, the use of SS-2D may also become even more relevant when one considers the inevitable loss of in-vessel sensors due to failures and ageing of components under the extreme neutron and radiation fluxes. Conversely, there is essentially no use for SS-2D in TCV, where the toroidal and poloidal arrays are exactly orthogonal, nor in JET, due to the extremely limited number of available sensors, which are furthermore too sparsely distributed.

The computational cost of SS-2D vs. 2xSS-H2 is however typically at least 10x higher if not more, and this makes it currently impossible to deploy SS-2D in real-time, contrary to the foreseen use of 2xSS-H2 for ITER analyses and makes it rather un-attractive for off-line routine analyses. The reason for the much higher computational requirements for SS-2D is straightforward. All 1D versions of the SparSpec algorithm (SS-H2 and the two variants of SS-V5) are based on the BCD algorithm, combined with the IRLS method. We could not find in the literature any approach that would allow us to adapt the 1D BCD and IRLS algorithms into numerically efficient 2D methods suited to the specific requirements of our measurement problem. Therefore, the practical solution was to transform our 2D problem into a 1D problem. This worked numerically at the expense however of having to use much larger matrices, with the ensuing much higher CPU and RAM requirements even for a very advanced and optimized language such as Matlab. If a suitably optimized and adapted 2D version of the BCD+IRLS algorithm could be obtained, then we would expect the CPU run-time for SS-2D to massively decrease.

Our final steps in the development of SparSpec are now that of implementing the error weighting of the penalization criterion (as per SS-V5b0) and then a memory and relaxation scheme (as per SS-V5) to improve the overall performance of the SS-2D algorithm. Based on our previous experience with the development from SS-H2 to SS-V5, we expect that these two steps could reduce the overall CPU run-time of SS-2D by a factor 3 to 5: SS-2D will still not be competitive with 2xSS-V5 (as this also

runs $\sim 3\text{-}5\times$ faster than SS-H2), but with a significantly reduced CPU run-time we expect that SS-2D will become more attractive for routine analyses, at least in the off-line environment.

Acknowledgements.

This work has been carried out within the framework of the EUROfusion Consortium, funded by the European Union via the Euratom Research and Training Programme (Grant Agreement No 101052200 — EUROfusion). Views and opinions expressed are however those of the author(s) only and do not necessarily reflect those of the European Union or the European Commission. Neither the European Union nor the European Commission can be held responsible for them. This work was also partly supported by the Swiss National Science Foundation. Finally, DTA would like to acknowledge the help of Dr. Christian Galperti (SPC-EPFL) in addressing certain subtleties with memory allocation when using function handles to run C++ codes within Matlab for timing purposes, and Dr. Matteo Vallar (SPC-EPFL) for the KINX analyses leading to producing figure 15 in this paper.

References

1. D.Testa, H.Carfantan, L.M.Perrone, *Plasma Research Express* **3** (2021), 025005; doi: <https://doi.org/10.1088/2516-1067/abf946>.
2. D.Testa, H.Carfantan, L.M.Perrone, *Plasma Research Express* **3** (2021), 025006; doi: <https://doi.org/10.1088/2516-1067/abf947>.
3. D.Testa, H.Carfantan, M.Albergante, P.Blanchard, S.Bourguignon, et al., *Plasma Physics and Controlled Fusion* **58** (2016), 123001; doi: <http://dx.doi.org/10.1088/0741-3335/58/12/123001>.
4. M.Sperl, *Communication in Asteroseismology* **111** (1998), 1.
5. J.Lafler, T.D.Kinman, *The Astrophysical Journal Supplement* **11** (1965), 216; <https://ui.adsabs.harvard.edu/abs/1965ApJS...11..216L/abstract>.
6. R.F.Stellingwerf, *The Astrophysical Journal* **224** (1978), 953.
7. M.M.Dworetzky, *Monthly Notice of the Royal Astronomical Society* **203** (1983), 917.
8. N.R.Lomb, *Astrophysics and Space Science* **39(2)** (1976), 447.
9. J.D.Scargle, *The Astrophysical Journal* **263** (1982), 835.
10. D.Roberts, J.Lehar, J.Dreher, *The Astronomical Journal* **93** (1987), 968.
11. D.F.Gray, K.Desikachary, *The Astrophysical Journal* **181** (1973), 523.
12. S.Mallat, Z.Zhang, *IEEE Transaction on Signal Processing* **41** (1993), 3397.
13. J.A.Högbom, *Astronomy and Astrophysics Supplement* **15** (1974), 417.
14. S.Bourguignon, H.Carfantan, T.Böhm, *Astronomy and Astrophysics* **462** (2007), 379; doi: <https://doi.org/10.1051/0004-6361:20065452>.
15. S.Bourguignon, H.Carfantan, J.Idier, *IEEE Journal of Selected Topics in Signal Processing* **1** (2007), 4; doi: <https://doi.org/10.1109/JSTSP.2007.910275>.
16. A.Klein, H.Carfantan, D.Testa, A.Fasoli, J.Snipes, *Plasma Physics and Controlled Fusion* **50** (2008), 125005; doi: <https://doi.org/10.1088/0741-3335/50/12/125005>.
17. D.Testa, H.Carfantan, R.Chavan, J.B.Lister, J-M.Moret, et al., *Fusion Science Technology* **57** (2010), 208-237 (<https://www.tandfonline.com/doi/abs/10.13182/FST10-A9468>); and 238-273 (<https://www.tandfonline.com/doi/abs/10.13182/FST10-A9469>).
18. D.Testa, H.Carfantan, A.Goodyear, P.Blanchard, A.Klein, et al., *Europhysics Letters* **92** (2010), 50001; doi: <http://dx.doi.org/10.1209/0295-5075/92/50001>.
19. D.Testa, A.Fasoli, A.Goodyear, Q.King, P.Blanchard, et al., *Fusion Engineering and Design* **86** (2011), 381-392; doi: <http://dx.doi.org/10.1016/j.fusengdes.2011.03.053>.
20. D.Testa, H.Carfantan, A.Goodyear, *Plasma and Fusion Research* **9** (2014), 1405003; http://www.jspf.or.jp/PFR/PFR_articles/pfr2014/pfr2014_09-1405003.html.
21. T.Panis, D.Testa, A.Fasoli, A.Klein, H.Carfantan, P.Blanchard, et al., *Nuclear Fusion* **50** (2010), 084019; doi: <http://dx.doi.org/10.1088/0029-5515/50/8/084019>.

22. D.Testa, N.Mellet, T.Panis, P.Blanchard, H.Carfantan, A.Fasoli, et al., Nuclear Fusion **50** (2010), 084010; doi: <http://dx.doi.org/10.1088/0029-5515/50/8/084010>.
23. T.Panis, A.Fasoli, D.Testa, Nuclear Fusion **52** (2012), 023013 (<http://dx.doi.org/10.1088/0029-5515/52/2/023013>) and 023014 (<http://dx.doi.org/10.1088/0029-5515/52/2/023014>).
24. D.Testa, T.Panis, P.Blanchard, A.Fasoli, Nuclear Fusion **52** (2012), 094006; doi: <http://dx.doi.org/10.1088/0029-5515/52/9/094006>.
25. D.Testa, P.Blanchard, T.Panis, Nuclear Fusion **55** (2015), 123010; doi: <http://dx.doi.org/10.1088/0029-5515/55/12/123010>.
26. P.Puglia, W.Pires de Sa, P.Blanchard, S.Dorling, S.Dowson, et al., Nuclear Fusion **56** (2016), 112020; doi: <http://dx.doi.org/10.1088/0029-5515/56/11/112020>.
27. D.Testa, work carried out in the framework of the F4E/ITER contract F4E-OPE-0883, currently scheduled to be completed in late 2021 with only the baseline version of the SparSpec algorithm (SS-H2) being deployed; work carried out with various colleagues from the CREATE (Naples, Italy) and ENEA (Frascati, Italy) institutions.
28. S.Sardy, A.G.Bruce, P.Tseng, *Block Coordinate Relaxation Methods for Nonparametric Wavelet Denoising*, Journal of Computational and Graphical Statistics **9** (2000), 361; doi: <https://doi.org/10.2307/1390659>s.
29. D.Testa, *Manufacturing, Installation, Commissioning and First Results with the 3D Low-Temperature Co-fired Ceramic High-Frequency Magnetic Sensors on the Tokamak à Configuration Variable*, Tutorial Paper in Review of Scientific Instruments **91** (2020), 081401; doi: <https://doi.org/10.1063/1.5115004>.
30. H.P.Furth, P.H.Rutherford, H.Selberg, *Tearing mode in the cylindrical tokamak*, The Physics of Fluids **16** (1973), 1054; doi: <https://aip.scitation.org/doi/10.1063/1.1694467>.
31. V.Merezhkin, *Structure of the magnetic-field perturbations in the disruptive instability in the T-6 tokamak*, Sov. Phys. JETP **4**, 152 (1978).
32. D.Testa, A.Fasoli, E.Solano, *Diagnosis and Study of Alfvén Eigenmodes Stability in JET*, Review Scientific Instruments **74** (2003), 1694; doi: <https://aip.scitation.org/doi/abs/10.1063/1.1534920>.
33. M.Baruzzo et al., *Fault analysis and improved design of JET in-vessel Mirnov coils*, Fusion Engineering and Design **150** (2020), 110863; <https://doi.org/10.1016/j.fusengdes.2019.02.123>.
34. S.Sharapov, D.Testa, et al., *MHD spectroscopy through detection detecting Toroidal Alfvén Eigenmodes and Alfvén wave cascades*, Phys. Lett. A **289** (2001), 127-134; doi: [https://doi.org/10.1016/S0375-9601\(01\)00588-6](https://doi.org/10.1016/S0375-9601(01)00588-6).
35. H.L.Berk et al., *Theoretical interpretation of Alfvén Cascades in tokamaks with a non-monotonic q-profile*, Phys. Rev. Lett. **87** (2001), 185002; <https://doi.org/10.1103/PhysRevLett.87.185002>.

36. F.Zonca et al., *Energetic particle mode stability in tokamaks with hollow q-profiles*, Physics of Plasmas **9** (2002), 4939; doi: <https://doi.org/10.1063/1.1519241>.
37. W.W.Heidbrink, H.H.Duong, J.Manson, E.Wilfrid, C.Oberman, *The nonlinear saturation of beam-driven instabilities: theory and experiment*, Physics of Fluids **B: Plasma Physics** **5** (1993), 2176; <https://doi.org/10.1063/1.860752>.
38. L.Stipani, D.Testa, A.Fasoli, M.Fontana, A.Karpushov, C.Marini, A.Merle, L.Porte, *Fishbone and de-trapping of fast ions during NBH discharges on TCV*, in Proceedings of the 15th IAEA TCM on Energetic Particles, Princeton (USA), 5-8 September 2017, edited by H.L.Berk and B.N.Breizman; pdf file available by request to the corresponding author(duccio.testa@epfl.ch).
39. L.Chen, R.B.White, M.N.Rosenbluth, *Excitation of Internal Kink Modes by Trapped Energetic Beam Ions*, Phys. Rev. Lett. **52** (1984), 1122; <https://doi.org/10.1103/PhysRevLett.52.1122>.
40. L.Degtyarev et al., *The KINX ideal MHD stability code for axisymmetric plasmas with separatrix*, Computer Physics Communication **103** (1997), 10.
41. ITER measurement specifications for the HF magnetic diagnostic system: System Design Description (DDD) 55.A0 Magnetic Diagnostics, document 3UYGX, dated 14.09.2015; pdf file available on request to the corresponding author (duccio.testa@epfl.ch).
42. Contract document for the F4E-ITER contract F4E-OPE-0883 for the development of quasi-RT software for the analysis of magnetic instabilities in ITER; pdf file available on request to the corresponding author (duccio.testa@epfl.ch).

Figure1a, D.Testa, J.Charrière, paper SparSpec2D-V1

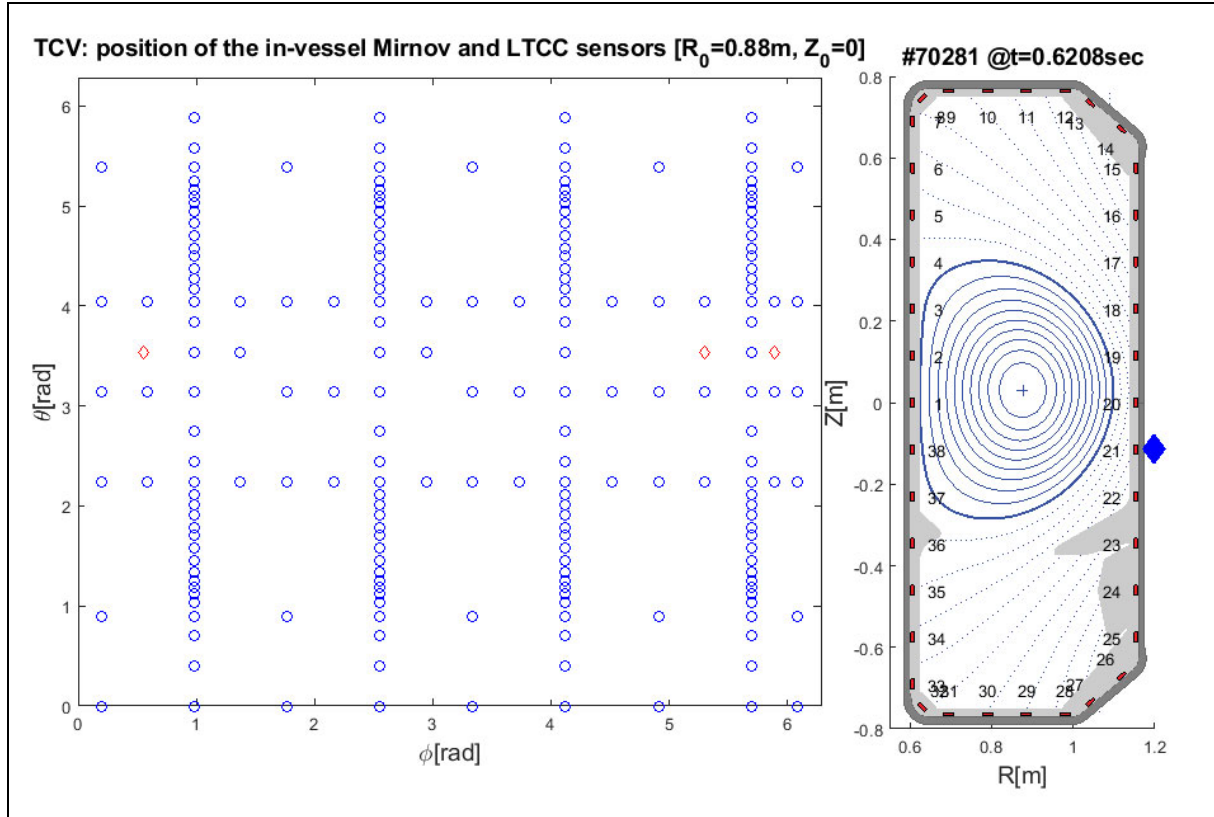


Figure1a. A schematic layout of the distribution of the HF magnetic sensors in the TCV tokamak. In TCV we have 38x Mirnov sensors each in four poloidal arrays, 17x sensors each in the three toroidal arrays on the low-field-side, and 8x sensors each in the three toroidal arrays on the high-field-side. Additionally, we also have 3x LTCC-3D sensors, acquired at a higher frequency. In the plot on the left, the blue dots are the Mirnov sensors, the red diamonds are the LTCC-3D sensors. The poloidal angle is determined using the geometrical centre of the machine (R_0, Z_0) and is oriented clock-wise, so that the values $\theta=\{0,\pi\}$ correspond to the midplane ($Z=Z_0$) on the HFS and on the LFS, respectively. The value $\phi=0$ corresponds to the weld attaching the first toroidal sector #1 to the last toroidal sector #16. In the plot on the right, the actual equilibrium for the TCV shot #70281 at $t=0.6208\text{sec}$ is used: the main equilibrium parameters are $B_{\phi 0}=-1.43\text{T}$, $I_p=-230\text{kA}$, $q_{\text{EDGE}}=4.15$, $\kappa_{\text{EDGE}}=1.32$, $\delta_{\text{TOP,EDGE}}=0.23$ and $\delta_{\text{BOT,EDGE}}=0.29$. The little red squares on the TCV wall show the poloidal position, with the corresponding labelling, of the 38x Mirnov sensors in the four toroidal sectors- $\{003,007,011,015\}$, i.e. those equipped with the full poloidal complement of magnetic sensors. The big blue diamond indicating the poloidal position of the LTCC-3D sensors has been slightly displaced outwards for clarity of plotting, as otherwise it would exactly overlap poloidally with the Mirnov sensor #21.

Figure1b, D.Testa, J.Charrière, paper SparSpec2D-V1

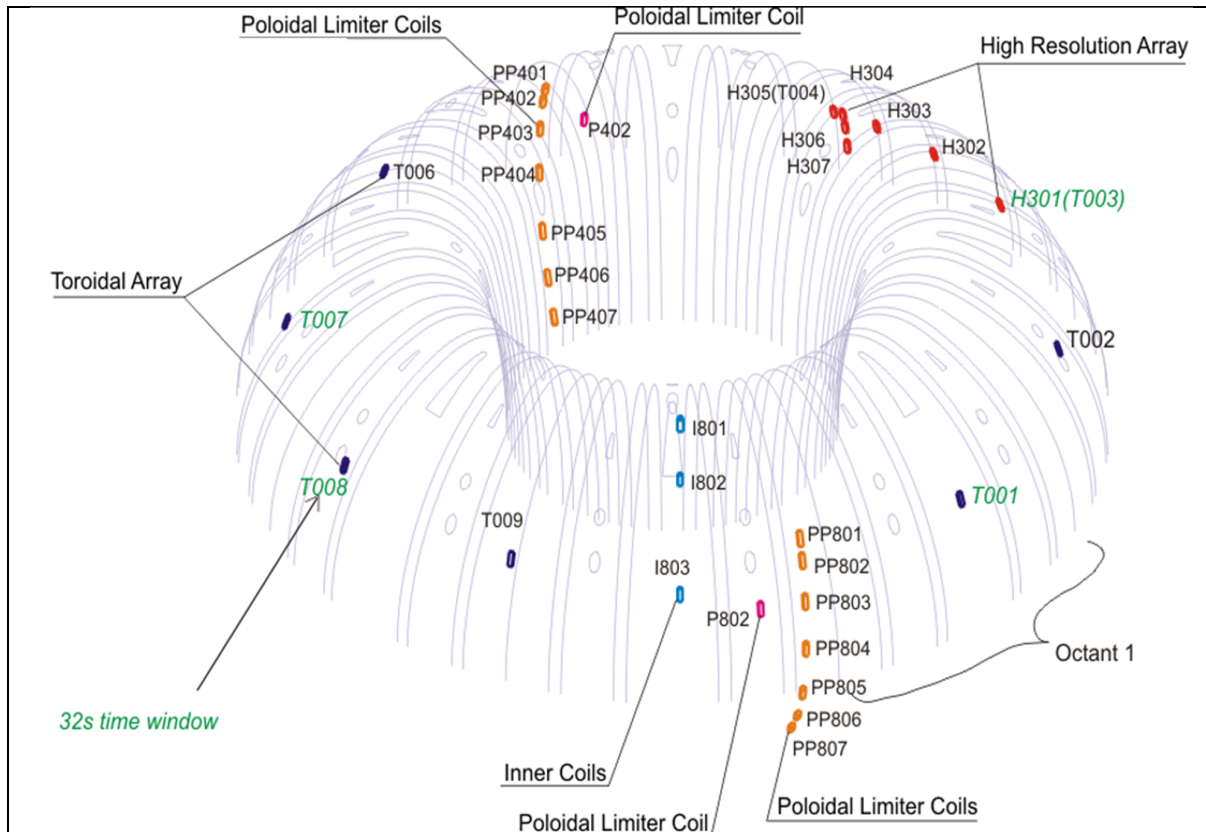


Figure1b. A schematic layout of the distribution of the HF magnetic sensors in the JET tokamak, i.e. those later used for the analyses reported in this and its two companion papers [1,2], together with a 3D folded view of the inner and the outer vessel structure. Different sets of HF magnetic sensors exist, for purely toroidal (the T-coils, the poloidal coordinate being the same for all of them, thus becoming ignorable) and purely poloidal (the PP-coils, the toroidal coordinate being the same for all of them, thus becoming ignorable) analyses, sitting on the inner (just a few, the purely poloidal I-coils) and the outer (most of them) vessel walls. Some of these sensors are positioned very close to each other to form a high-resolution array (the H-coils) with 8 sensors: when all the H-coils are used concurrently, there is no more an ignorable coordinate, and therefore this array could become suitable for combined toroidal and poloidal analyses.

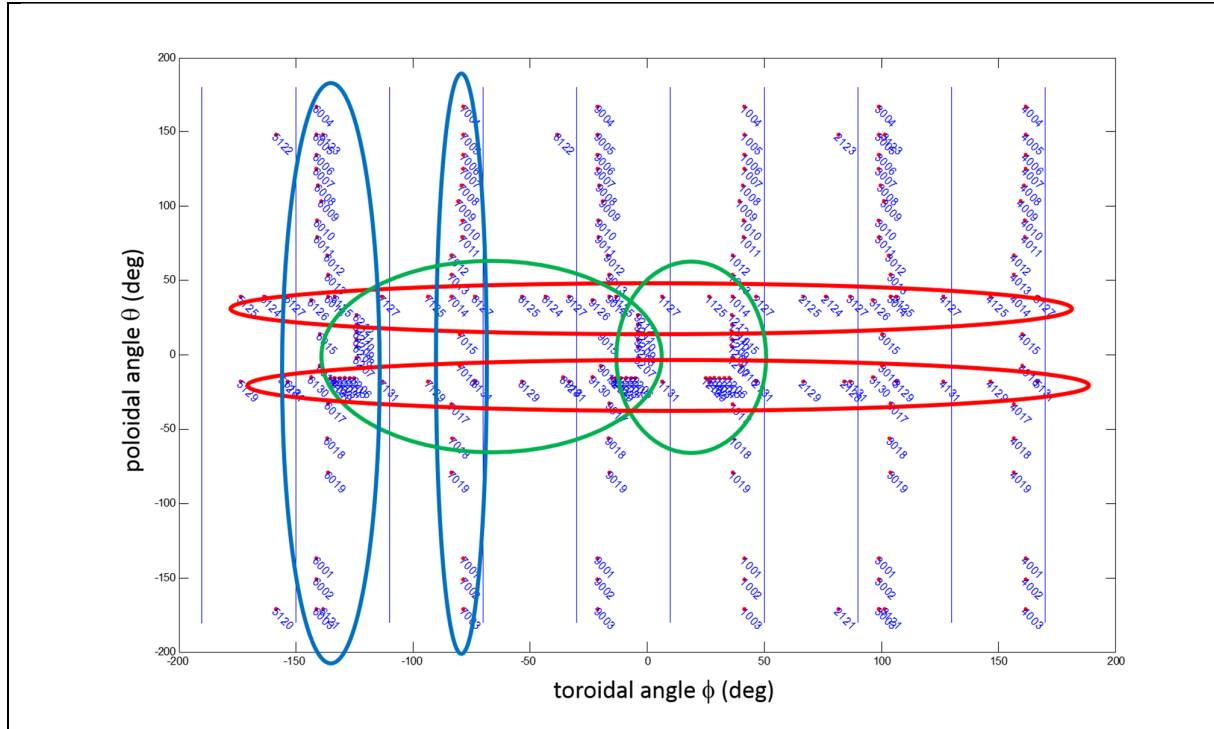


Figure1c. A schematic layout of the intended (i.e. as currently designed) distribution of the HF magnetic sensors in the ITER tokamak. As in TCV, most of the different poloidal and toroidal arrays are almost exactly orthogonal (for instance, those highlighted by the *red* and *blue* contours), but a subset of high-resolution sensors can be found for which both coordinates are not-ignorable (for instance, those highlighted with the green contours), as in JET. Highlighted in red and blue are the four groups of sensors that are currently intended to be used for the 1D toroidal (2x red) and poloidal (2x blue) analyses, respectively. The main difference between the two sets of the same colour is that one has NOT, while the other HAS, high-resolution (i.e. tightly spaced) sensors. The bottom red toroidal array sits at the nominal $\theta_{\text{GEOM}} = -30^\circ$ (i.e. determined using the geometric centre of the machine) and has 41 non equi-spaced sensors not all sitting exactly at the same θ_{GEOM} . The top red toroidal array sits at the nominal $\theta_{\text{GEOM}} = +30^\circ$ and has 30 non equi-spaced sensors, without high-resolution ones. In both red arrays there is a subset of 18 equi-spaced ones sitting at the same θ_{GEOM} . The blue poloidal array sitting at $\phi \sim -120^\circ$ has 24 sensors, including some high-resolution ones. The blue poloidal array sitting at $\phi \sim -80^\circ$ has 19 sensors, without high-resolution ones. For both poloidal arrays the sensors do not sit all exactly at the same ϕ . Finally, the two groups of *green* sensors are those selected for the 2D analyses, have 37 and 24 sensors each, and both include two sets of high-resolution sensors; the main geometrical difference between them is that one covers a larger toroidal extent, $\sim 120^\circ$ compared to $\sim 30^\circ$.

Figure2a, D.Testa, J.Charrière, paper SparSpec2D-V1

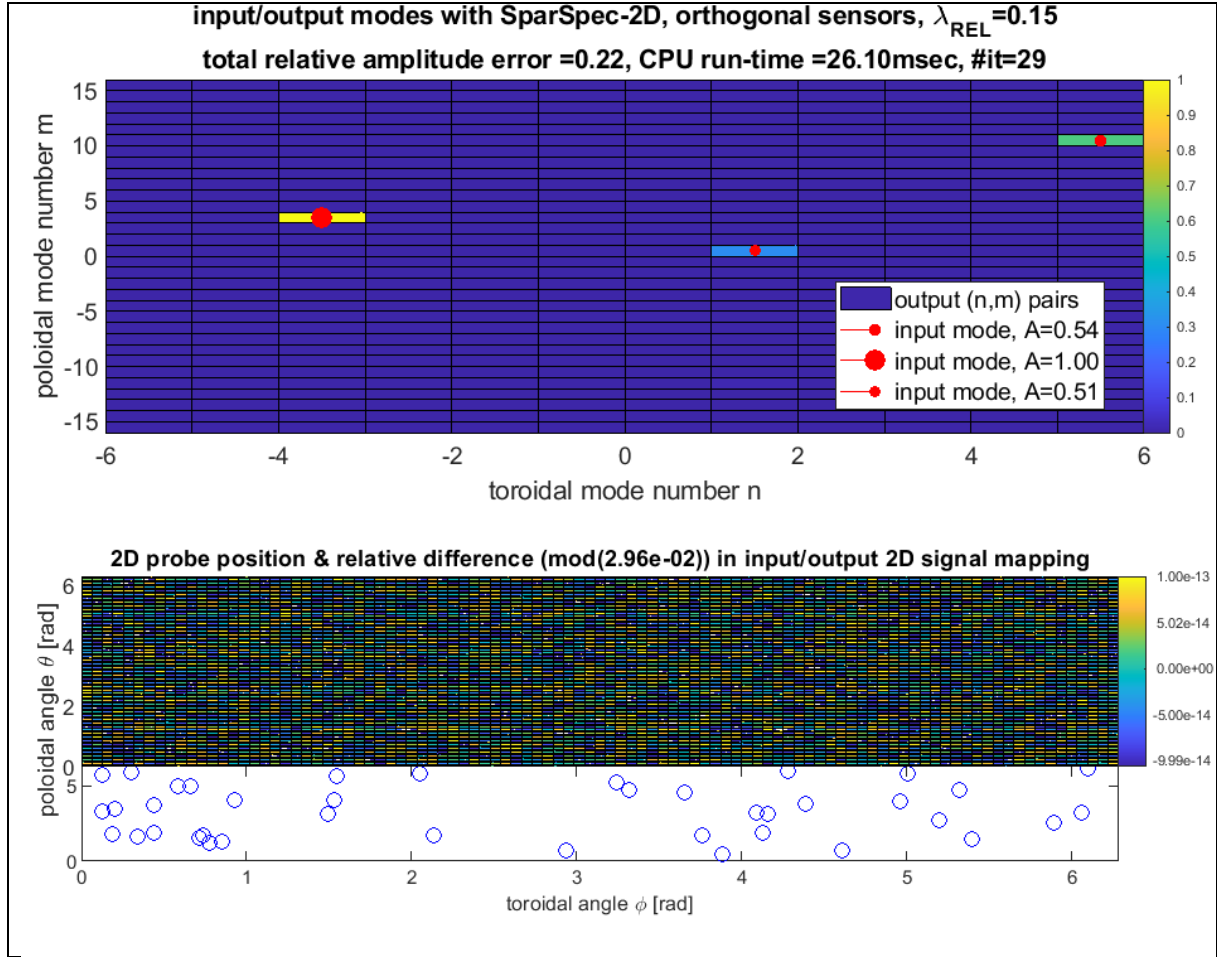


Figure2a. An illustrative example of a single test run for SparSpec-2D using $N_{SENS}=40$ randomly distributed and (quasi-)orthogonal sensors (thus with a (quasi-)ignorable coordinate). For this test run we have used $N_{COMP}=3=M_{COMP}$, $\lambda_{REL}=0.15$, $\max(\{\delta_k/\pi, \sigma_k, \sigma_l\})=0.15$, $N_{MAX}=5$, $M_{MAX}=15$ and $F_{maxS}\{N,M\}=5 \times \{N,M\}_{MAX}$. The bottom frame shows the spatial distribution of the sensors, the middle frame the relative difference in the input vs. output 2D signal mapping. The top frame shows the input components with red filled circles, whose size is proportional to the mode amplitude, while the background image shows the output signal components, whose amplitude is color-coded by the colorbar. For this test run, all input components are correctly detected, thus producing a rather small error on the overall energy conservation, but the computational cost is high.

Figure2b, D.Testa, J.Charrière, paper SparSpec2D-V1

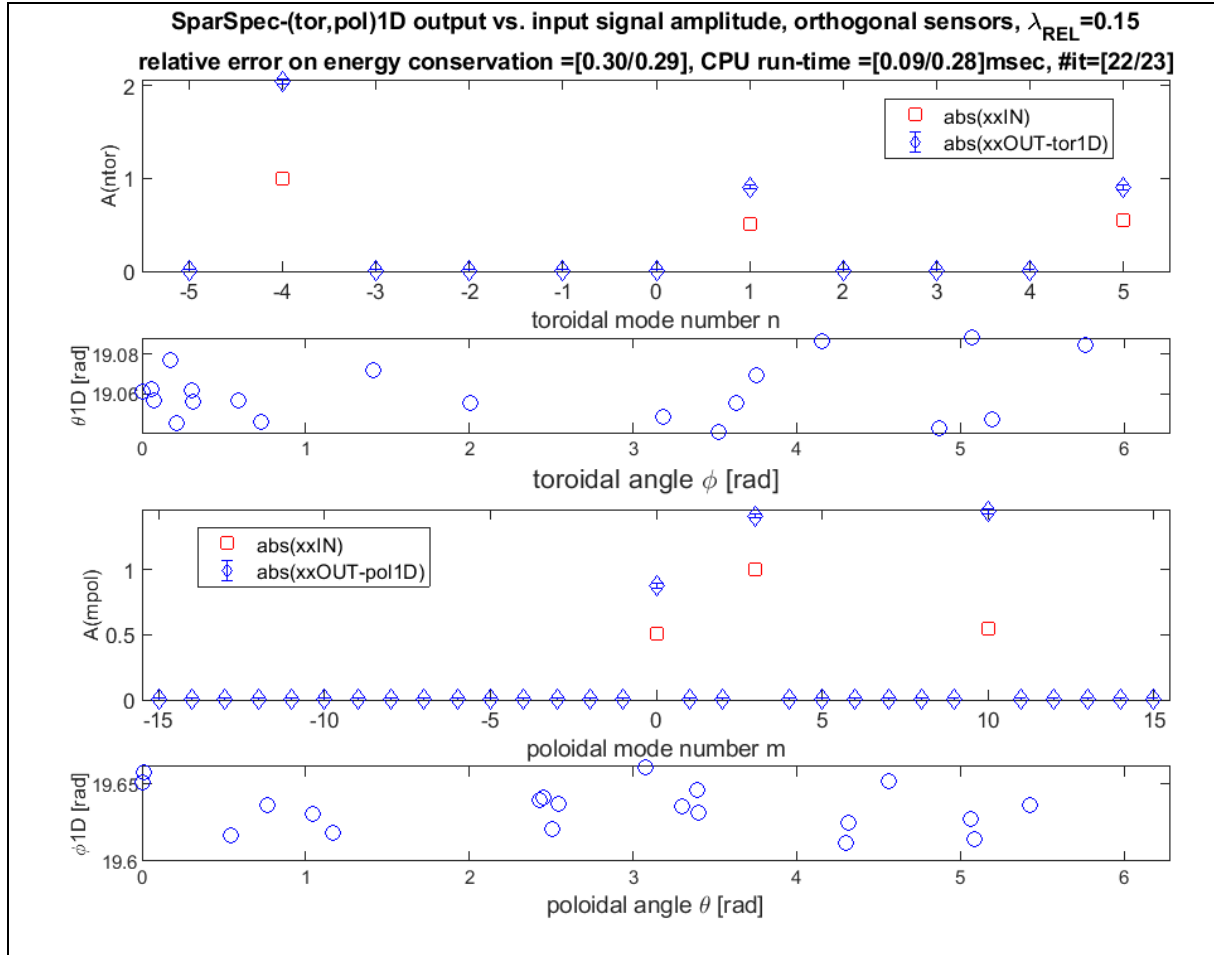


Figure2b. The same analysis as in fig2a but now using two separate runs of SS-H2, for the toroidal and poloidal 1D analyses, respectively. The two bottom frames show the results of the poloidal analyses, respectively the sensors distribution and the output vs. input mode amplitudes. The two top frames show the corresponding results for the toroidal analyses. The accuracy of the results is excellent considering that the (toroidal, poloidal) sensors are not exactly aligned at $\{\theta=0, \phi=0\}$: the relative error on the energy conservation and on the output vs. input mode amplitudes is essentially due to not respecting this condition of exact orthogonality. Note the much shorter computational time of SS-H2 with respect to SS-2D, a fraction of a millisecond compared to >25 msec.

Figure3a, D.Testa, J.Charrière, paper SparSpec2D-V1

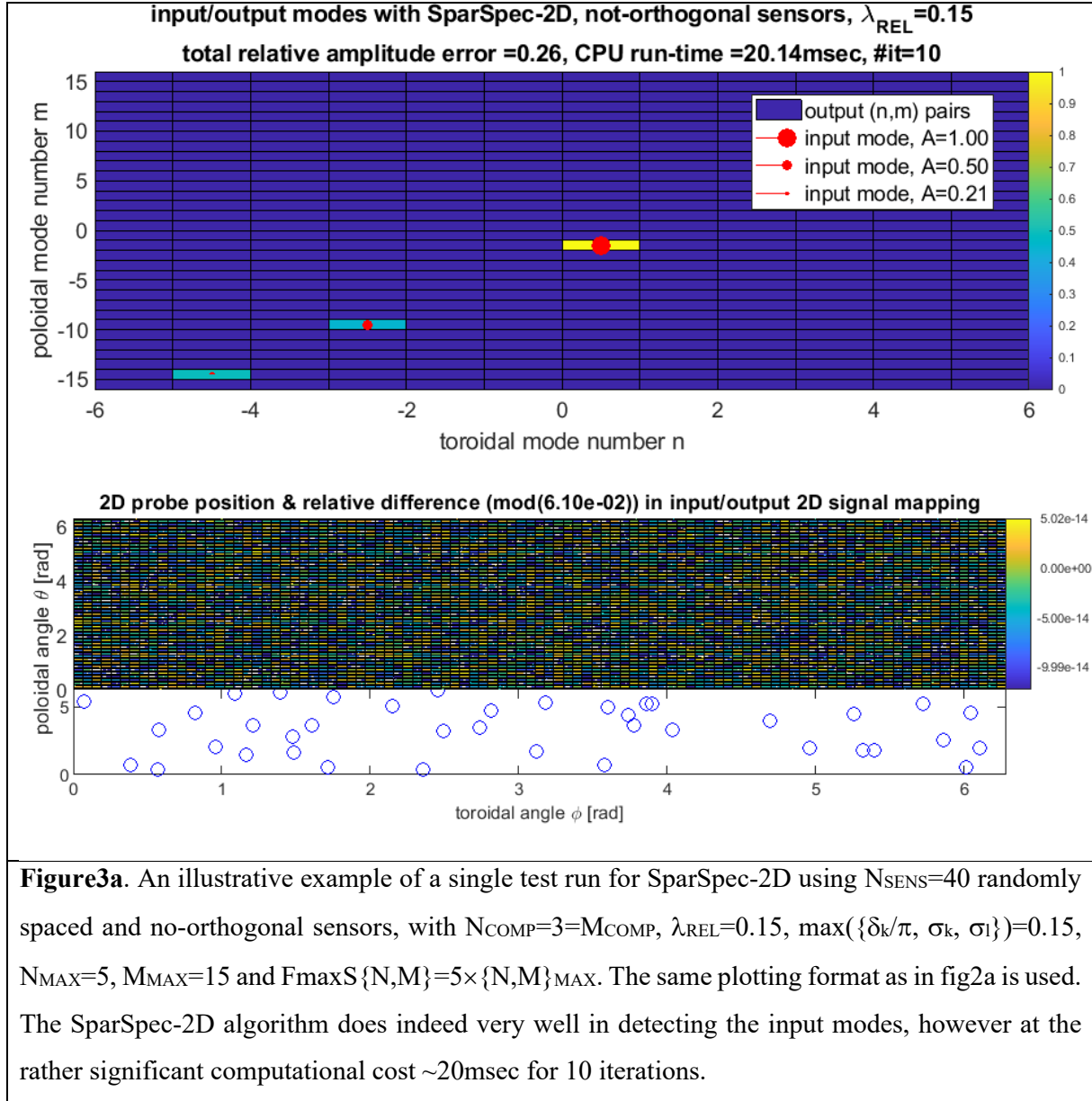


Figure3a. An illustrative example of a single test run for SparSpec-2D using $N_{SENS}=40$ randomly spaced and no-orthogonal sensors, with $N_{COMP}=3=M_{COMP}$, $\lambda_{REL}=0.15$, $\max(\{\delta_k/\pi, \sigma_k, \sigma_l\})=0.15$, $N_{MAX}=5$, $M_{MAX}=15$ and $F_{maxS}\{N,M\}=5 \times \{N,M\}_{MAX}$. The same plotting format as in fig2a is used. The SparSpec-2D algorithm does indeed very well in detecting the input modes, however at the rather significant computational cost ~ 20 msec for 10 iterations.

Figure3b, D.Testa, J.Charrière, paper SparSpec2D-V1

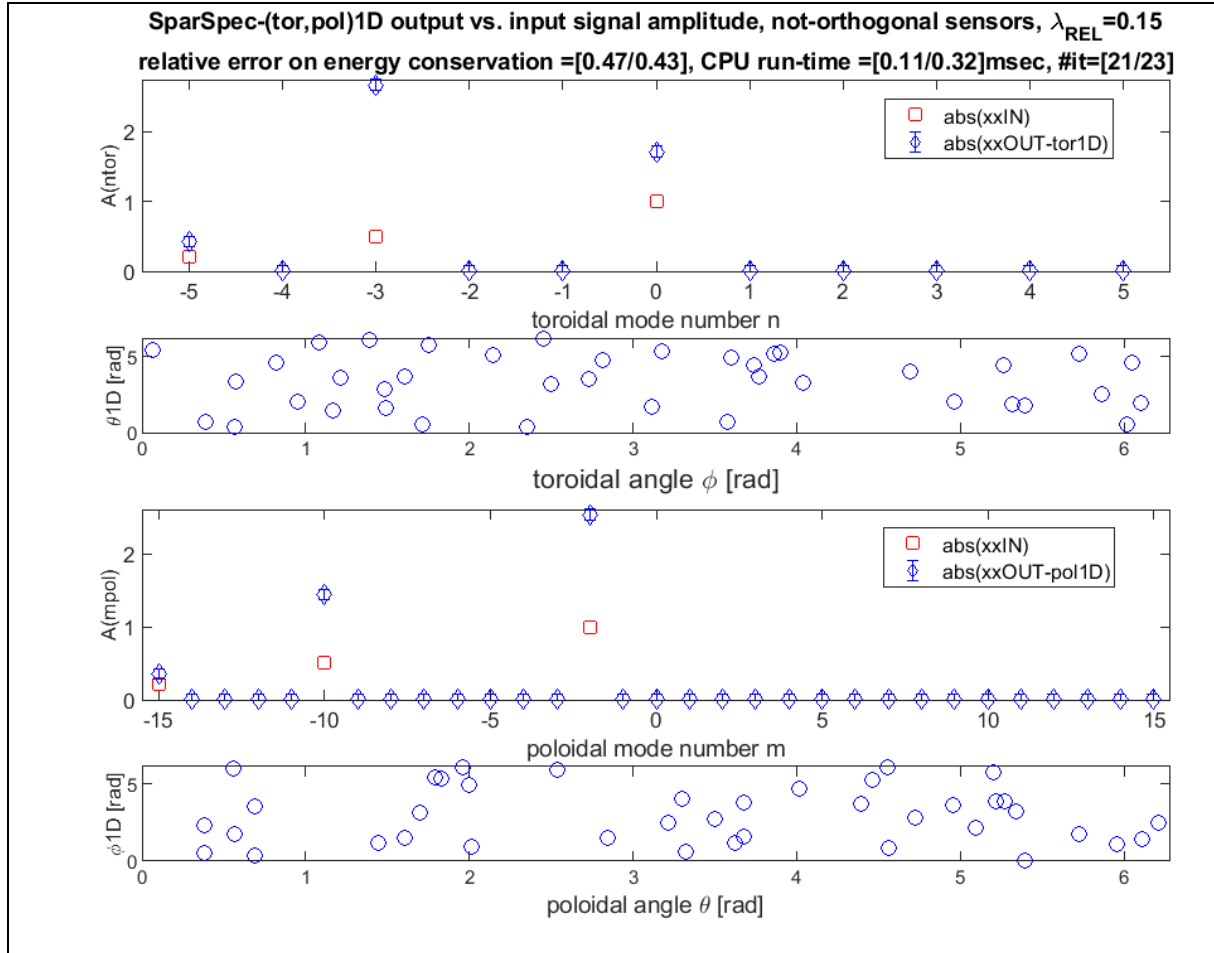


Figure3b. The same analysis as in fig3a but now using two separate runs of SS-H2, for the toroidal and poloidal 1D analyses, respectively; the plotting format is the same as in fig2b. Now there is a large discrepancy in the output vs. the input mode amplitudes, for both the poloidal and toroidal components, but the mode number is still correctly detected for all the toroidal and poloidal components. The computational cost is still very low, a fraction of a millisecond for ~ 20 iterations for each SS-H2 analyses compared to ~ 20 msec for 10 iterations for the SS-2D analysis. Therefore, it is clear that only when needing to correctly detecting the mode amplitudes, and not solely the mode numbers, SS-2D does a much better job than 2xSS-1D, and thus should be preferably used.

Figure4, D.Testa, J.Charrière, paper SparSpec2D-V1

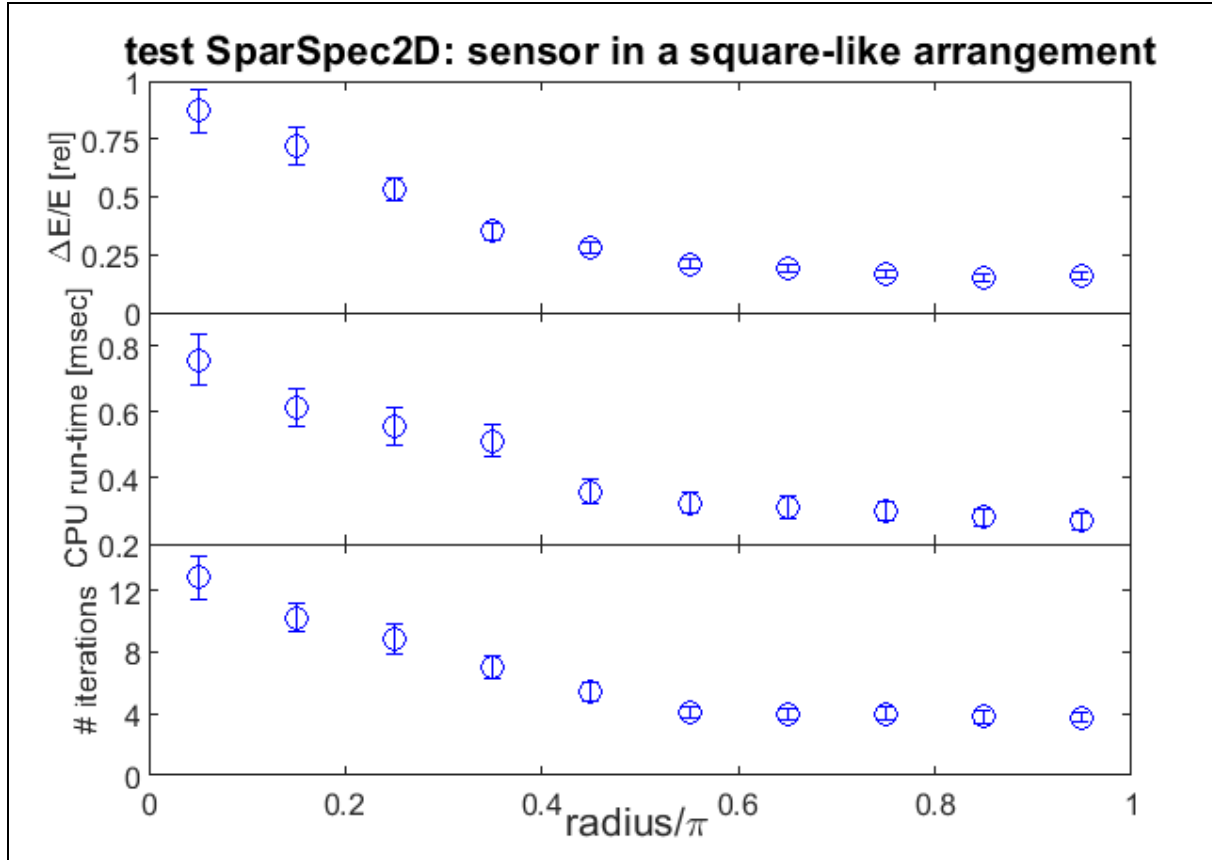


Figure4. An illustrative example of the SS-2D results for a specific sensor arrangement: a square of varying half-length for each side. This analysis was performed for a single set of test modes: $(n_1, m_1)=(2,0)$, $(n_2, m_2)=(2,4)$ and $(n_3, m_3)=(3,-3)$, all with amplitude $A_0=1$, always using $N_{\text{SENS}}=40$ randomly spaced sensors. For this test run $N_{\text{COMP}}=3=M_{\text{COMP}}$, $\lambda_{\text{REL}}=0.15$ and $\max(\{\sigma_k, \sigma_l\})=0.15$ randomized at each run, and $N_{\text{MAX}}=6$ $M_{\text{MAX}}=15$, $F_{\text{maxS}}\{N, M\}=5 \times \{N, M\}_{\text{MAX}}$ were used. Finally, 100 iterations were run for each value of the radius. It is clear that for this specific test case at least $R/\pi > 0.4$ is needed to obtain sufficiently accurate results in a sufficiently short computational time, and that going beyond $R/\pi > 0.65$ does not bring much further improvements in the accuracy and speed of the calculations.

Figure5, D.Testa, J.Charrière, paper SparSpec2D-V1

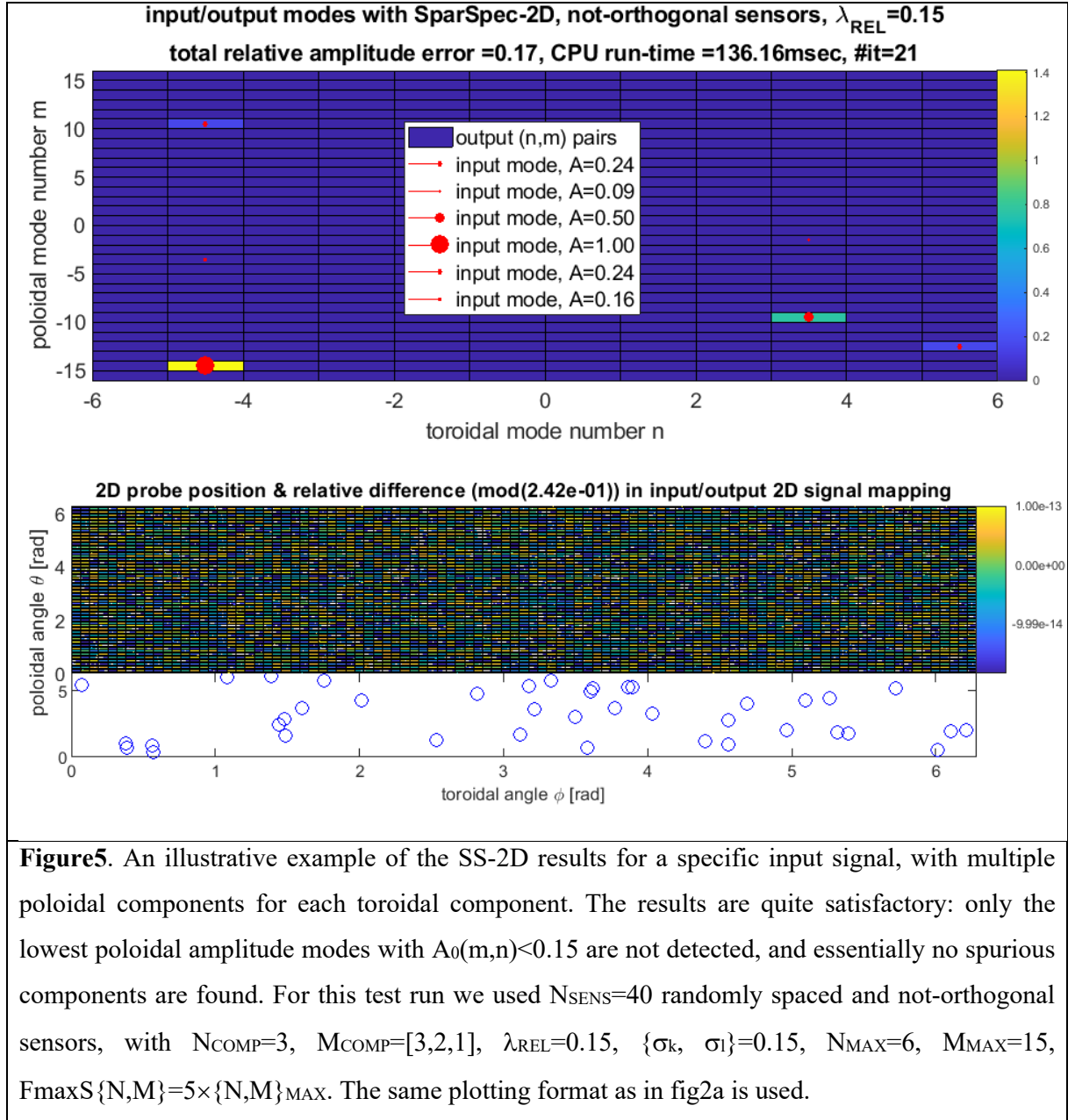


Figure6, D.Testa, J.Charrière, paper SparSpec2D-V1

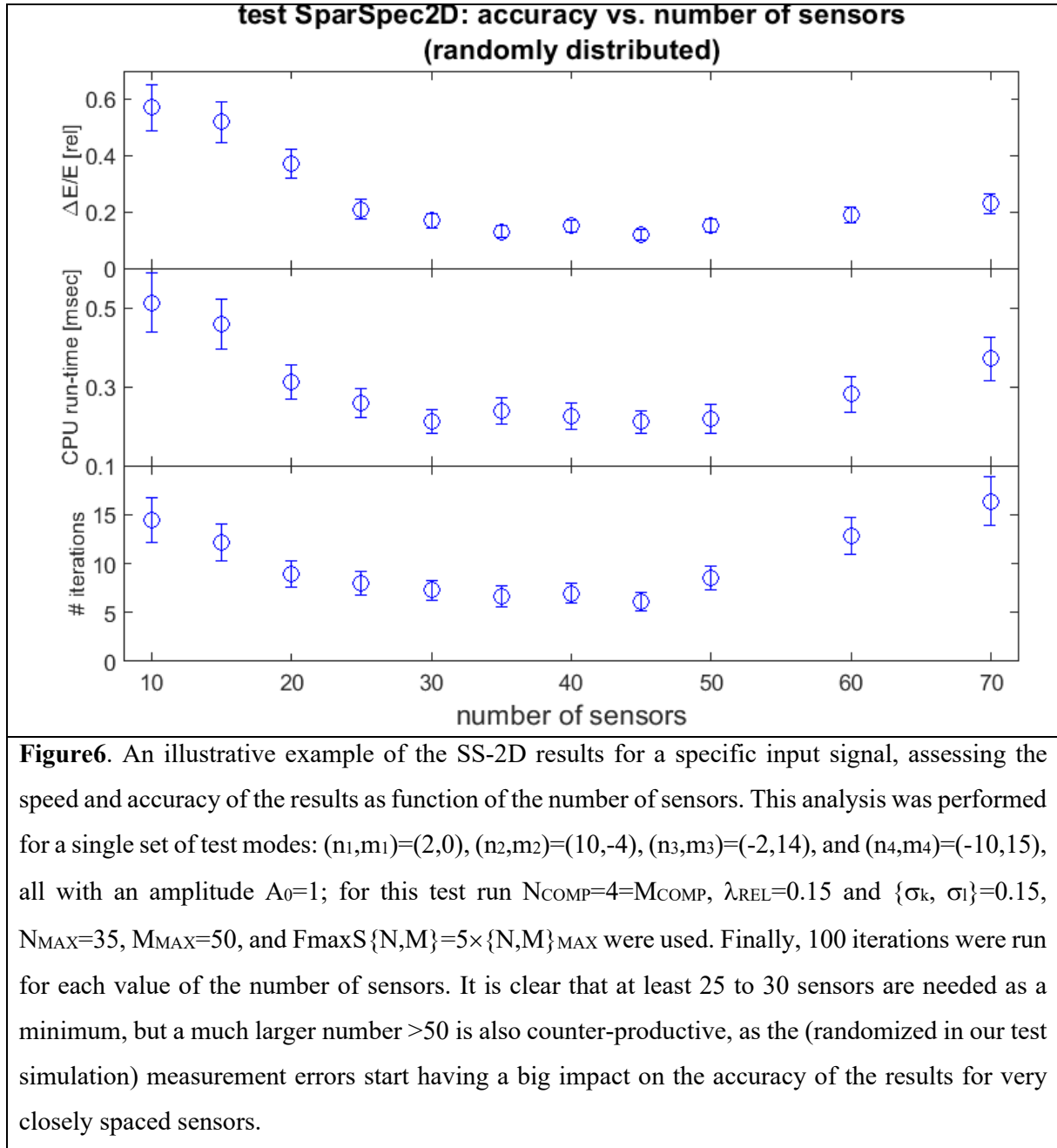


Figure7, D.Testa, J.Charrière, paper SparSpec2D-V1

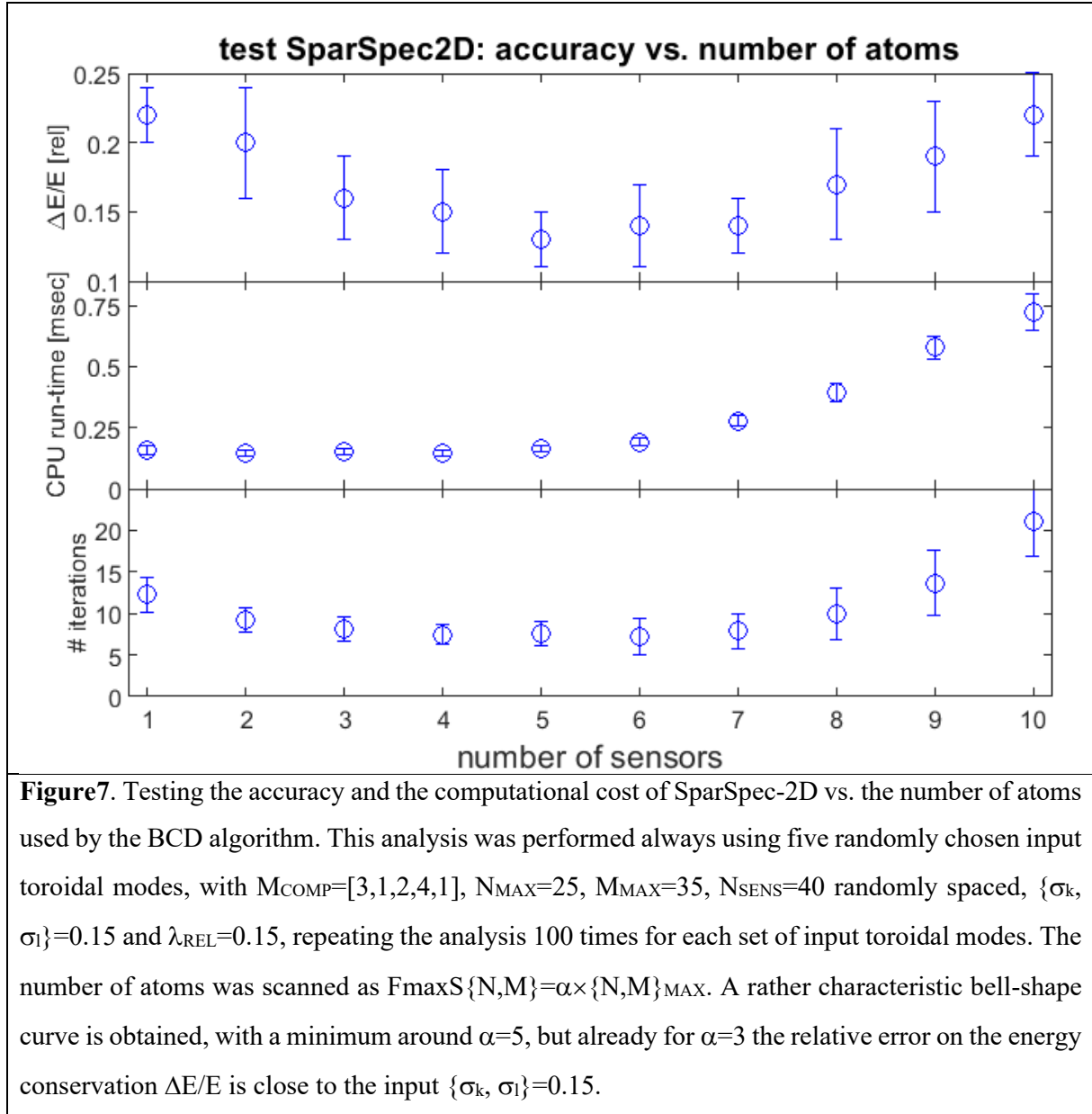


Figure8, D.Testa, J.Charrière, paper SparSpec2D-V1

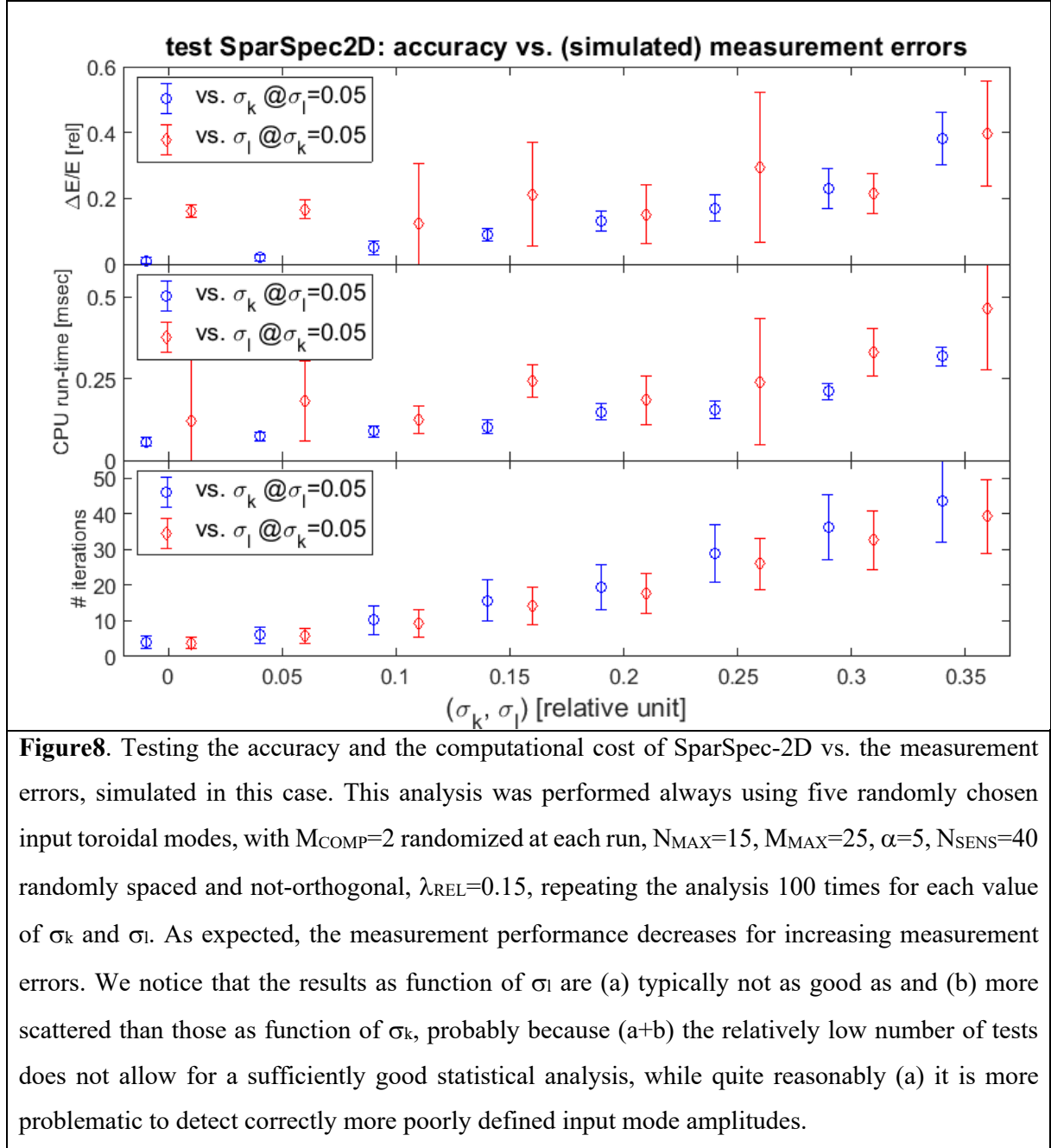


Figure9a, D.Testa, J.Charrière, paper SparSpec2D-V1

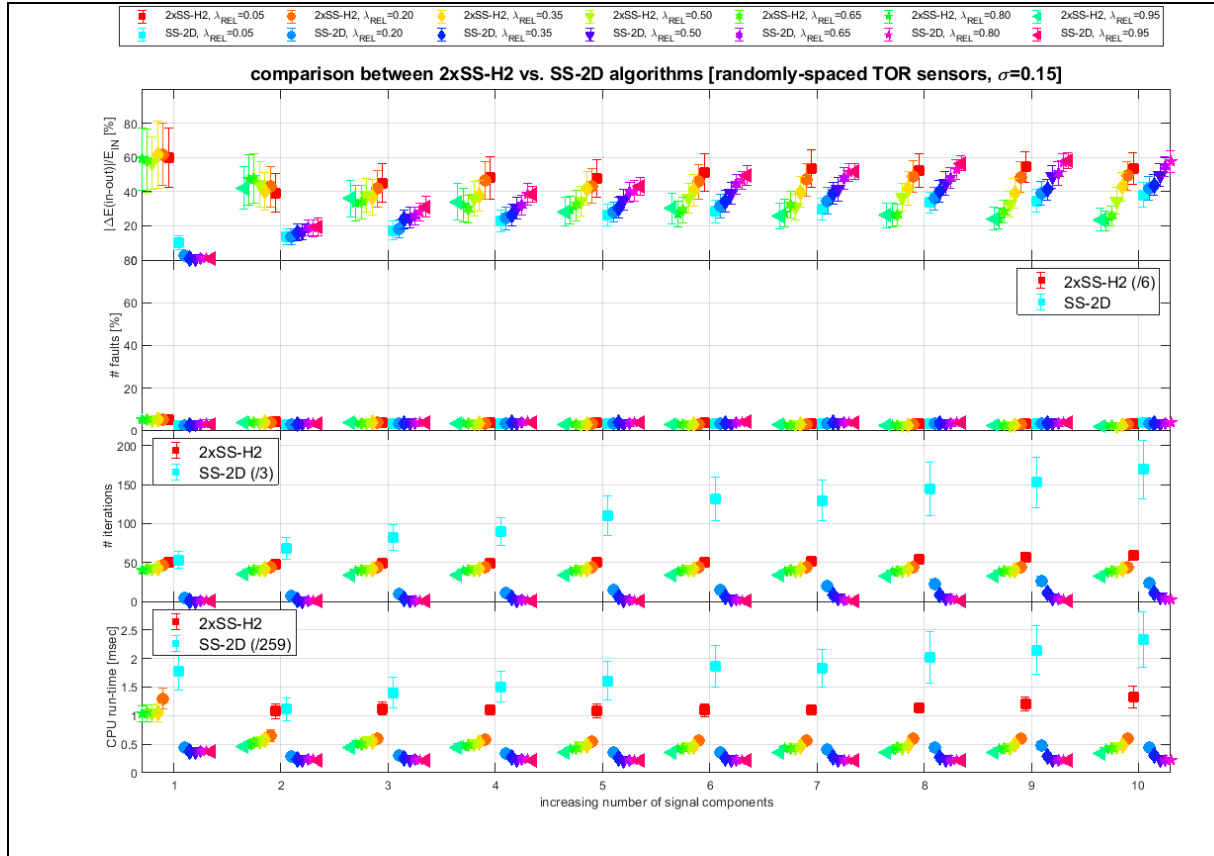


Figure9a. Testing the accuracy and the computational cost of SS-2D vs. 2xSS-H2 as function of λ_{REL} for $N_{COMP}=1 \rightarrow 10$ at fixed $M_{COMP}=N_{COMP}$. For this run we have used $N_{SENS}=40$ randomly distributed toroidal sensors, $N_{MAX}=35$ and $M_{MAX}=50$, $\max(\{\sigma_k, \sigma_l\})=0.15$ (in relative units), $\{\delta_k\} \in 0.2 \times \pi$, $F_{maxS}\{N,M\}=3 \times \{N,M\}_{MAX}$, $n_{IT}=1000$ and $TR_{IT}=1 \times 10^{-5}$. The results presented here are the RMS and STD values over 10'000 runs for each value of $\{N_{COMP}, \lambda_{REL}\}$. The number of faults is typically 6x lower for SS-2D than for 2xSS-H2, a clear improvement in the performance. The results are more complex to interpret for the energy conservation: we find that for a sufficiently low number of components, up to $N_{COMP}=3$, SS-2D clearly out-performs 2xSS-H2 for all values of λ_{REL} ; however, for $N_{COMP}>5$ the SS-2D results are much less convincing. Note in any case the significantly larger CPU run-time requirements for SS-2D.

Figure9b, D.Testa, J.Charrière, paper SparSpec2D-V1

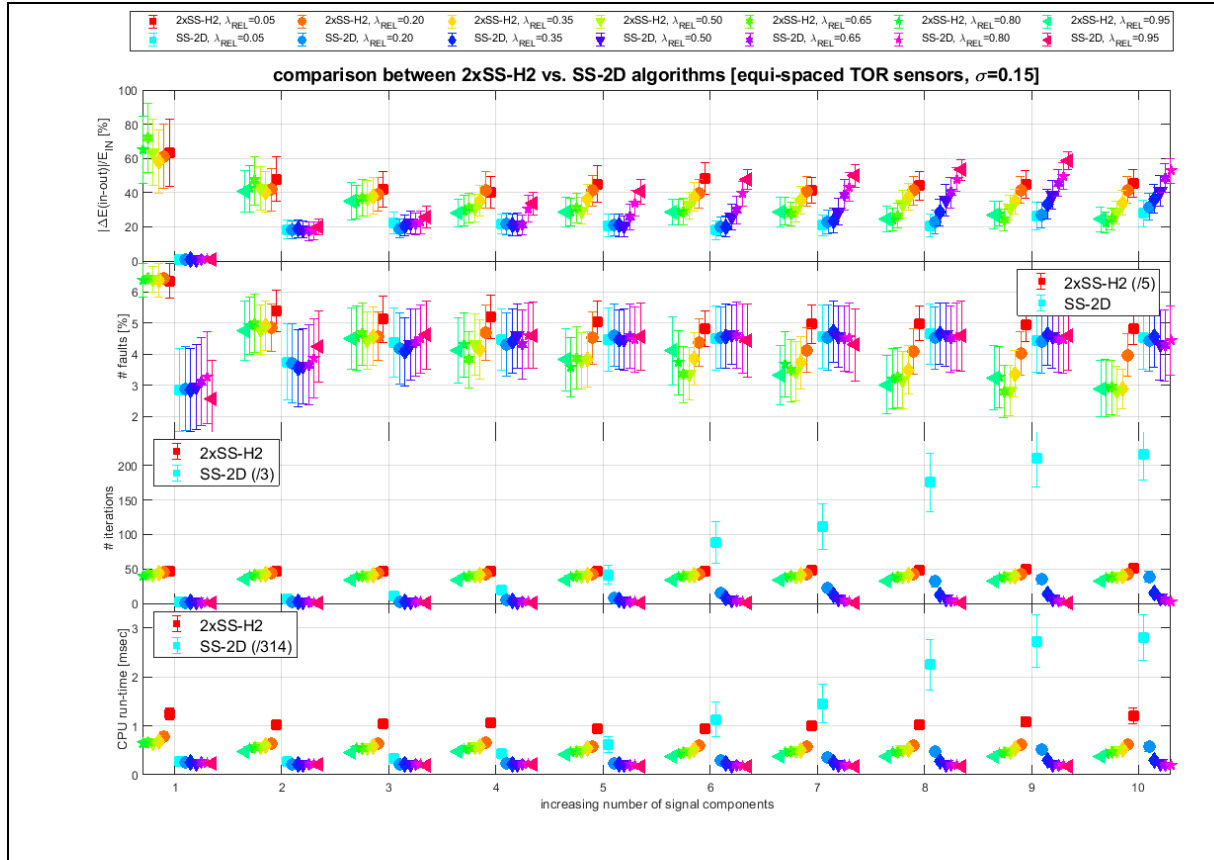


Figure9b. As in fig9a but now using $N_{SENS}=40$ equi-spaced toroidal sensors: the results are quite similar, which again points to SS-2D being useful essentially for a low number of input components up to $N_{COMP}=5$ at the most, practically irrespectively of the arrangement of toroidal sensors. The only clear difference in the SS-2D performance between using randomly vs. equi-spaced toroidal sensors is the CPU run-time, significantly longer in the latter case.

Figure10, D.Testa, J.Charrière, paper SparSpec2D-V1

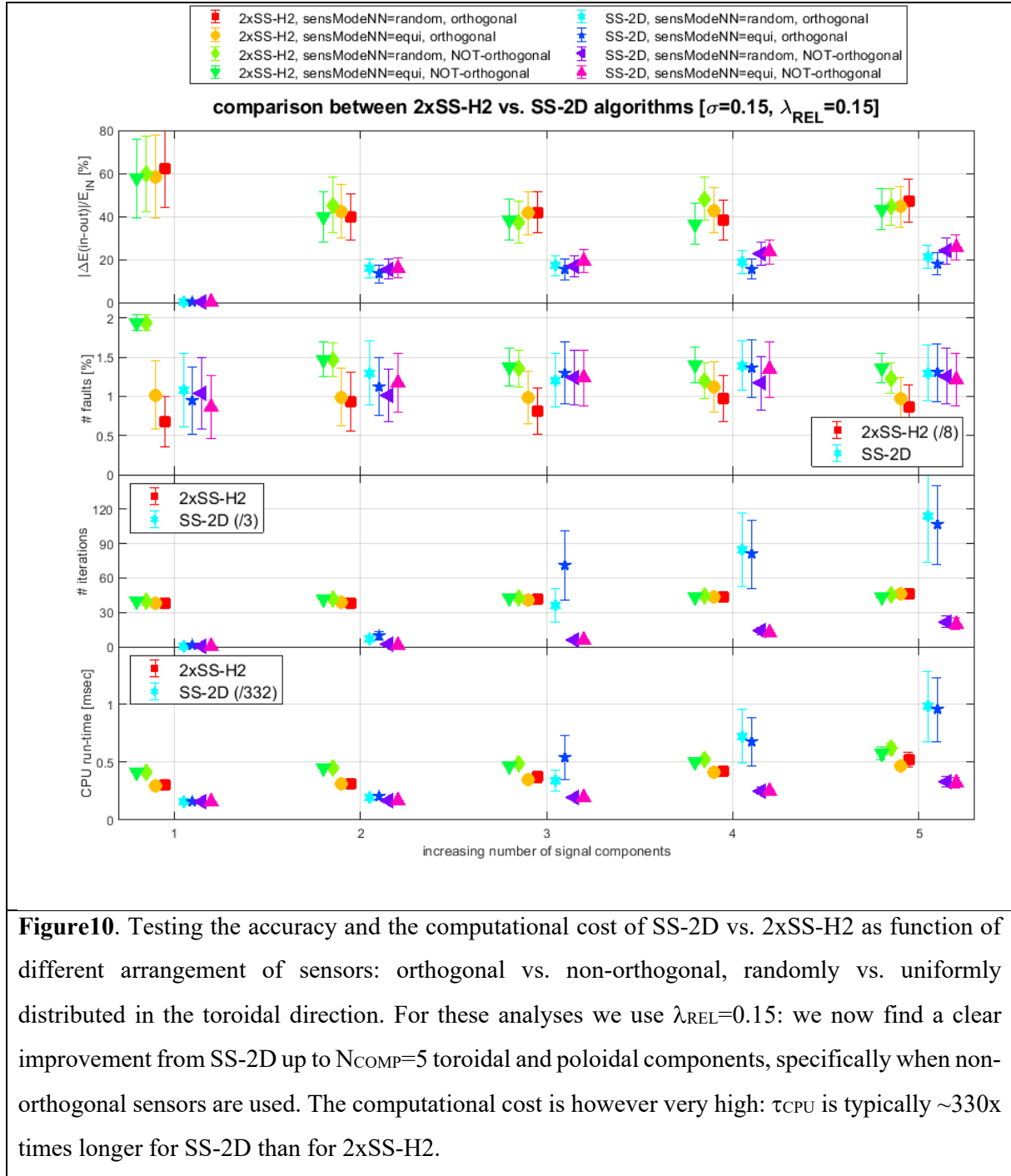


Figure11, D.Testa, J.Charrière, paper SparSpec2D-V1

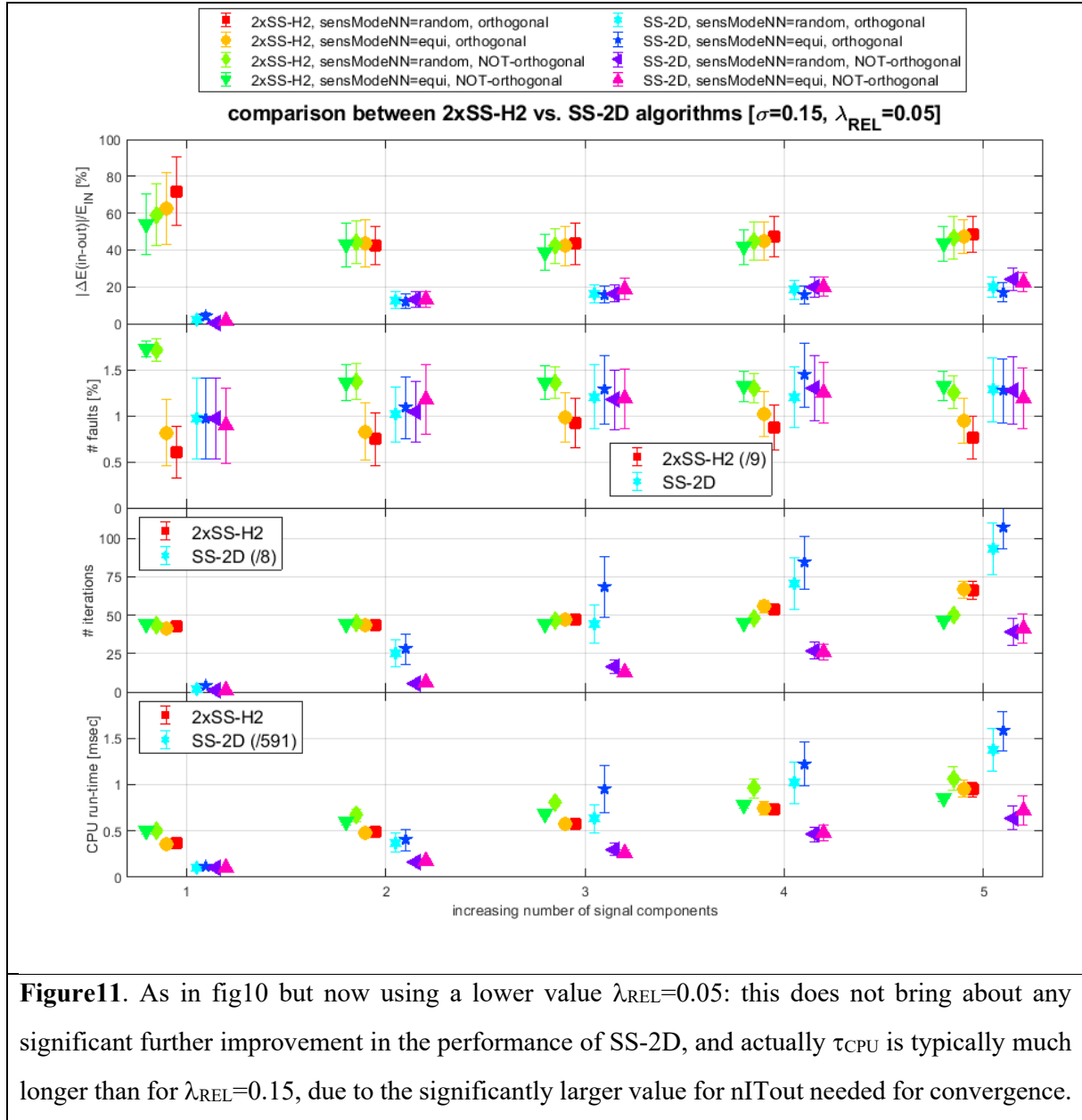


Figure11. As in fig10 but now using a lower value $\lambda_{REL}=0.05$: this does not bring about any significant further improvement in the performance of SS-2D, and actually τ_{CPU} is typically much longer than for $\lambda_{REL}=0.15$, due to the significantly larger value for nITout needed for convergence.

Figure12, D.Testa, J.Charrière, paper SparSpec2D-V1

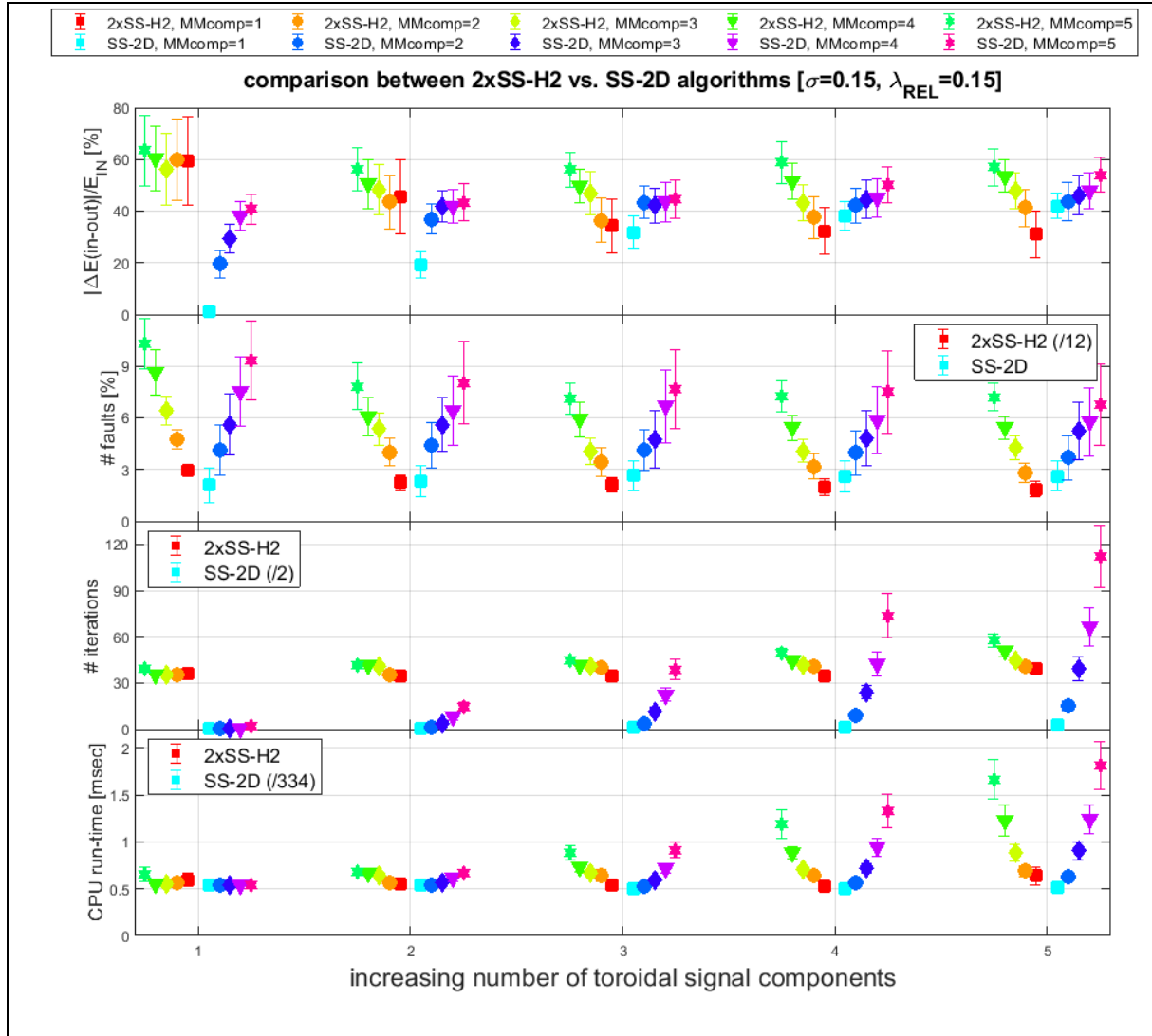


Figure12. Testing the accuracy and the computational cost of SS-2D vs. 2xSS-H2 as function of the number of poloidal components for each toroidal mode, using only randomly distributed and non-orthogonal sensors. Now it is very clear where the main advantage of SS-2D is with respect to 2xSS-H2: in tokamaks we typically have multiple poloidal components for a single toroidal mode, and SS-2D definitively out-performs 2xSS-H2 for the analyses of this experimental situation. The computational cost is however very high, but the accuracy is significantly improved with the SS-2D analyses. The deterioration of the performance of SS-2D for $N_{COMP}>3$ and $M_{COMP}>3$ is probably due to RAM limitations in the laptop used for these simulations, so that only $\alpha=3$ could be used.

Figure13(a,b), D.Testa, J.Charrière, paper SparSpec2D-V1

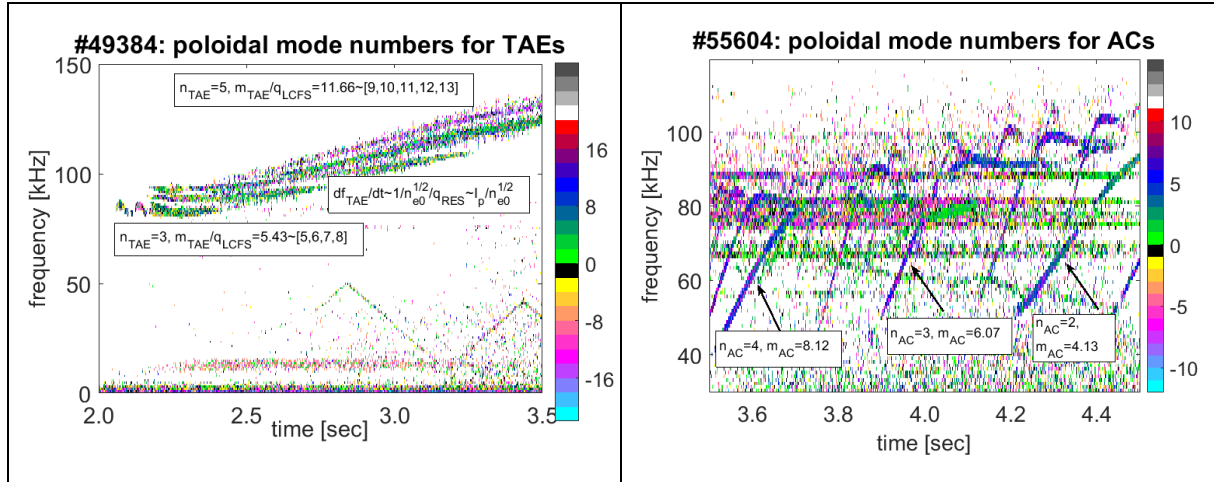


Figure13(a,b). The spectrograms, annotated for clarity of interpretation, for the poloidal mode number for the JET shots #49384 (fig13a) and #55604 (fig13b), obtained using SS-2D and the H30N high resolution toroidal and poloidal sensors. For the TAEs in #49384 (fig13a) the value of the measured apparent poloidal mode number is scaled in the annotation through q_{LCFS} to provide an estimate of m_{TAE} at q_{RES} . We find that multiple poloidal harmonics exist for each one of the toroidal mode numbers $n_{TAE}=3 \rightarrow 5$ for the measured modes, and the resulting weighted value $m_{TAE} = \Sigma(m_{POL} \times A_{POL}^2) / \Sigma A_{POL}^2$ annotated in the spectrogram is rather far away from an integer. This can somewhat also be seen directly in the spectrogram, as the colour coding for the mode changes with time, indicating that different poloidal harmonics become dominant as the discharge evolves, due to the evolution of the current profile, hence q_{LCFS} . Conversely, for the ACs in #55604 (fig13b) we essentially find one largely dominant poloidal mode number, and thus (a) the weighted average is much closer to an integer, and (b) the colour coding for the modes does not really change with time, consistently with (a).

Figure14, D.Testa, J.Charrière, paper SparSpec2D-V1

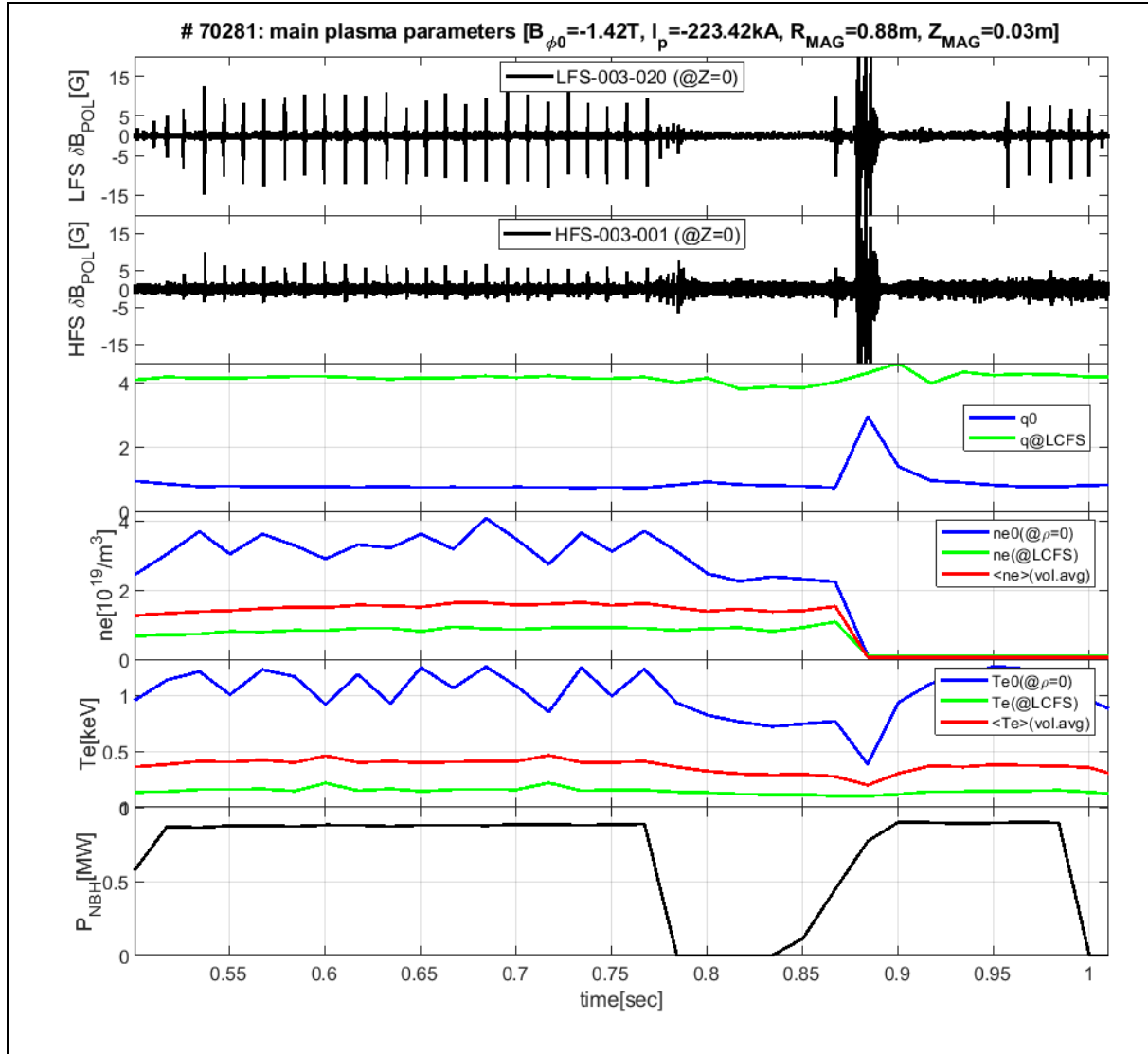


Figure14. The main background plasma parameters and two illustrative magnetic traces for the TCV shot #70281, showing the characteristic bursting behaviour of the sawbones. The frequency spectrum and the toroidal and poloidal mode structure of the sawbone starting at $t=0.6213\text{s}$ is then analysed in more details in fig16. The amplitude of the sawbones on the time trace is typically $\sim 15\text{G}$ -peak on the LFS vs. $\sim 5\text{G}$ -peak on the HFS, which indicates that these are pressure-driven modes stabilized by the curvature of the magnetic field. The major event at $t=0.87\text{s}$ is a partial disruption deliberately triggered via the notch in the NBH power for RT control purposes.

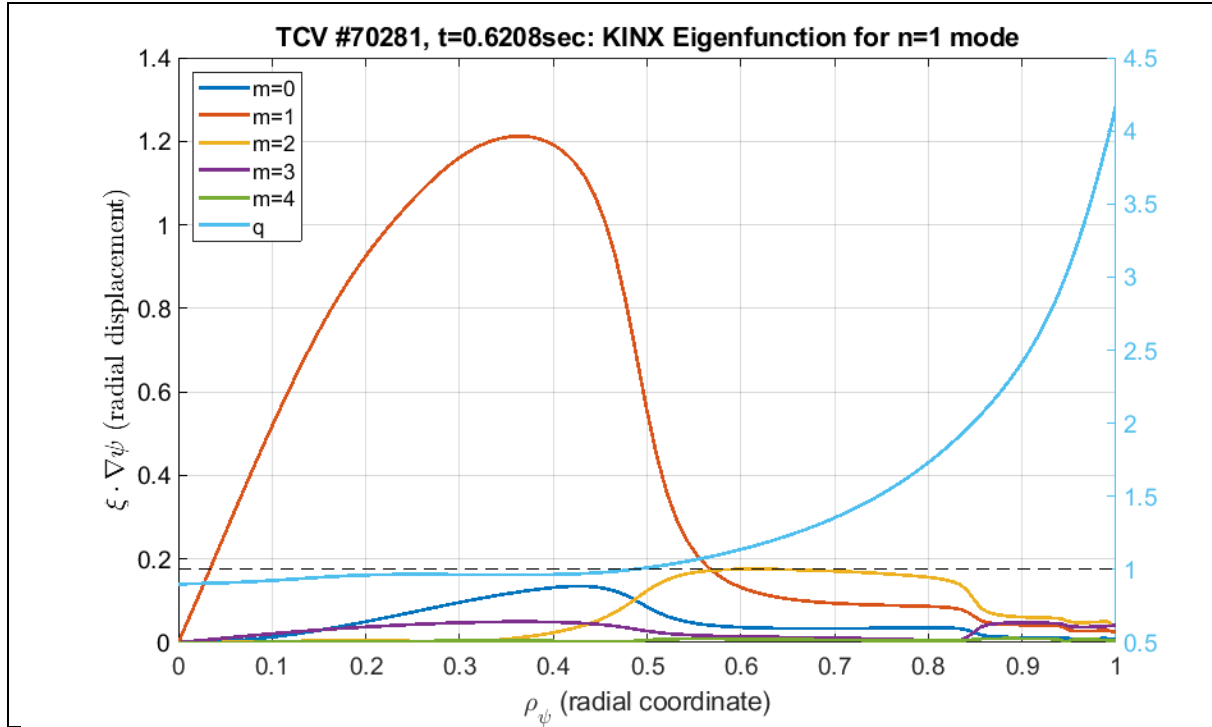


Figure15. The poloidal mode structure for the $n=1$ mode, calculated using the KINX code at $t=0.6208\text{sec}$, which is the equilibrium time point closest to the onset of the sawbone at $t=0.6213\text{sec}$. While the dominant poloidal harmonic at the resonant q -surface is $m_{\text{RES}}=1$, as naturally expected, the poloidal mode structure changes appreciably over the poloidal cross-section. At the plasma edge the dominant poloidal harmonics are $m=2$ and $m=3$, with an approximately equal amplitude, and there is still a significant $m=1$ component. It is therefore only natural, although very often misunderstood as an error in the analyses, that the magnetic sensors located at the wall will measure an apparent poloidal mode number m_{MEAS} different from the resonant one m_{RES} .

[KINX analyses and figure courtesy of Dr. Matteo Vallar, SPC-EPFL].

Figure16, D.Testa, J.Charrière, paper SparSpec2D-V1

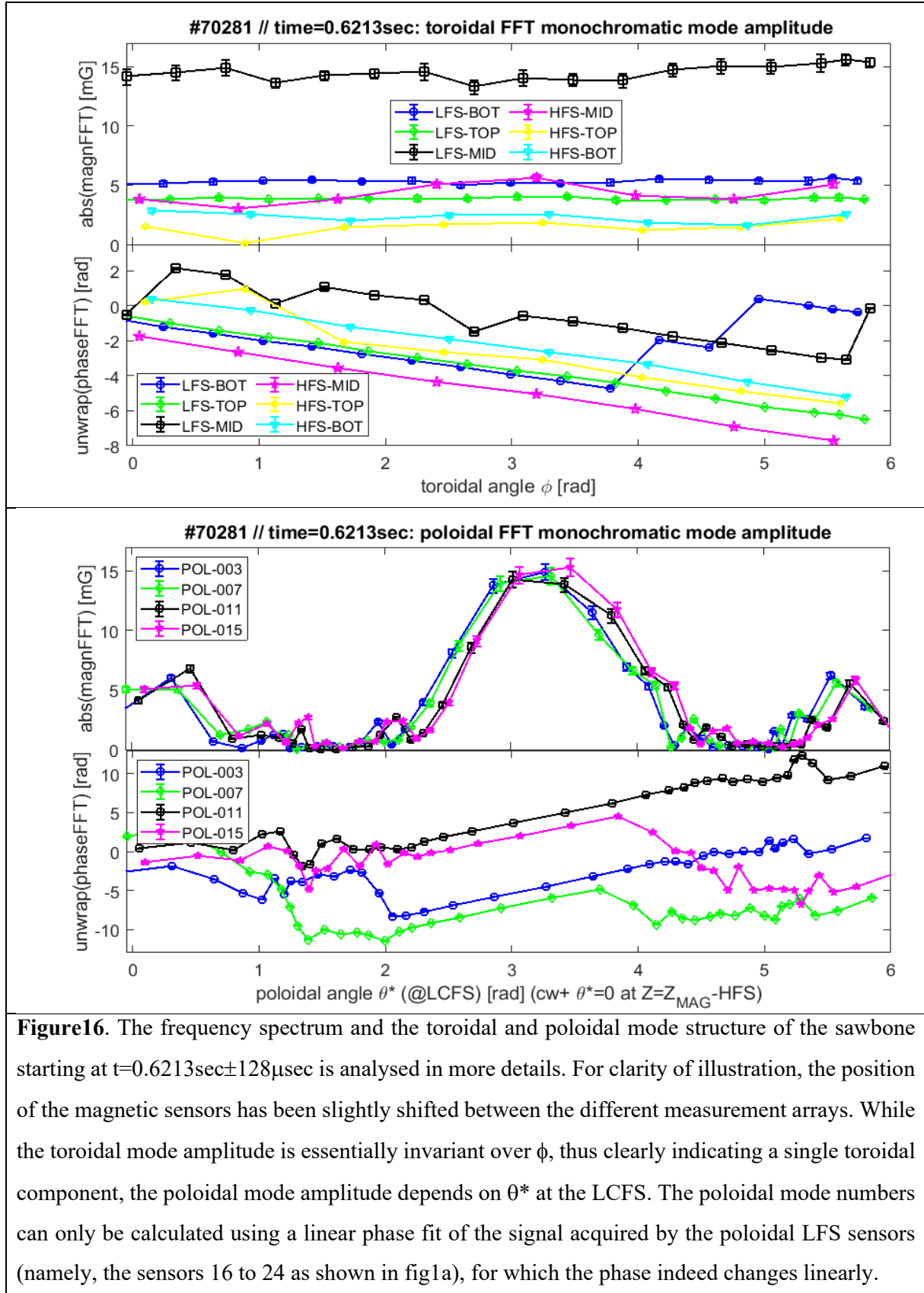


Figure17a, D.Testa, J.Charrière, paper SparSpec2D-V1

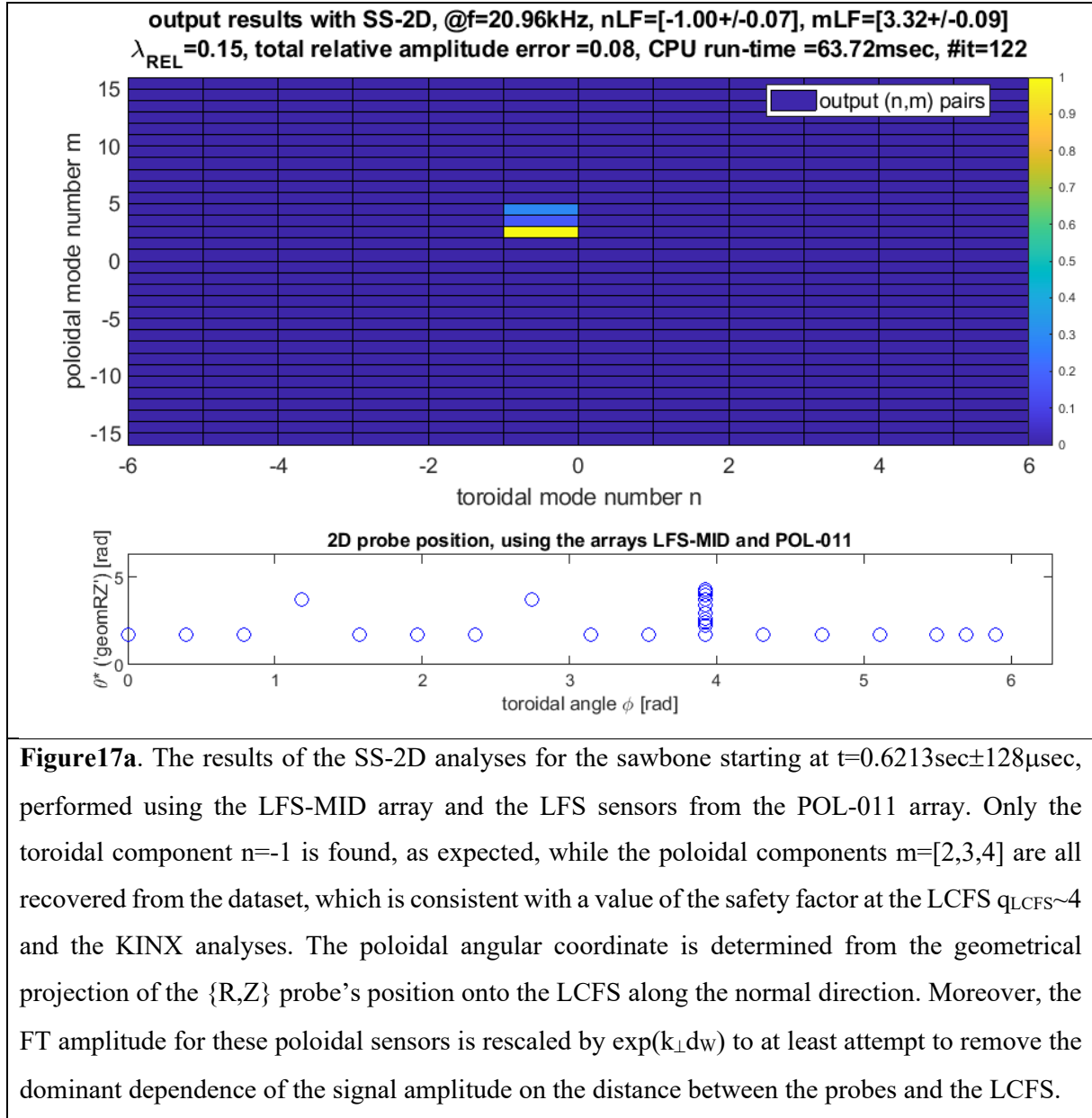


Figure17b, D.Testa, J.Charrière, paper SparSpec2D-V1

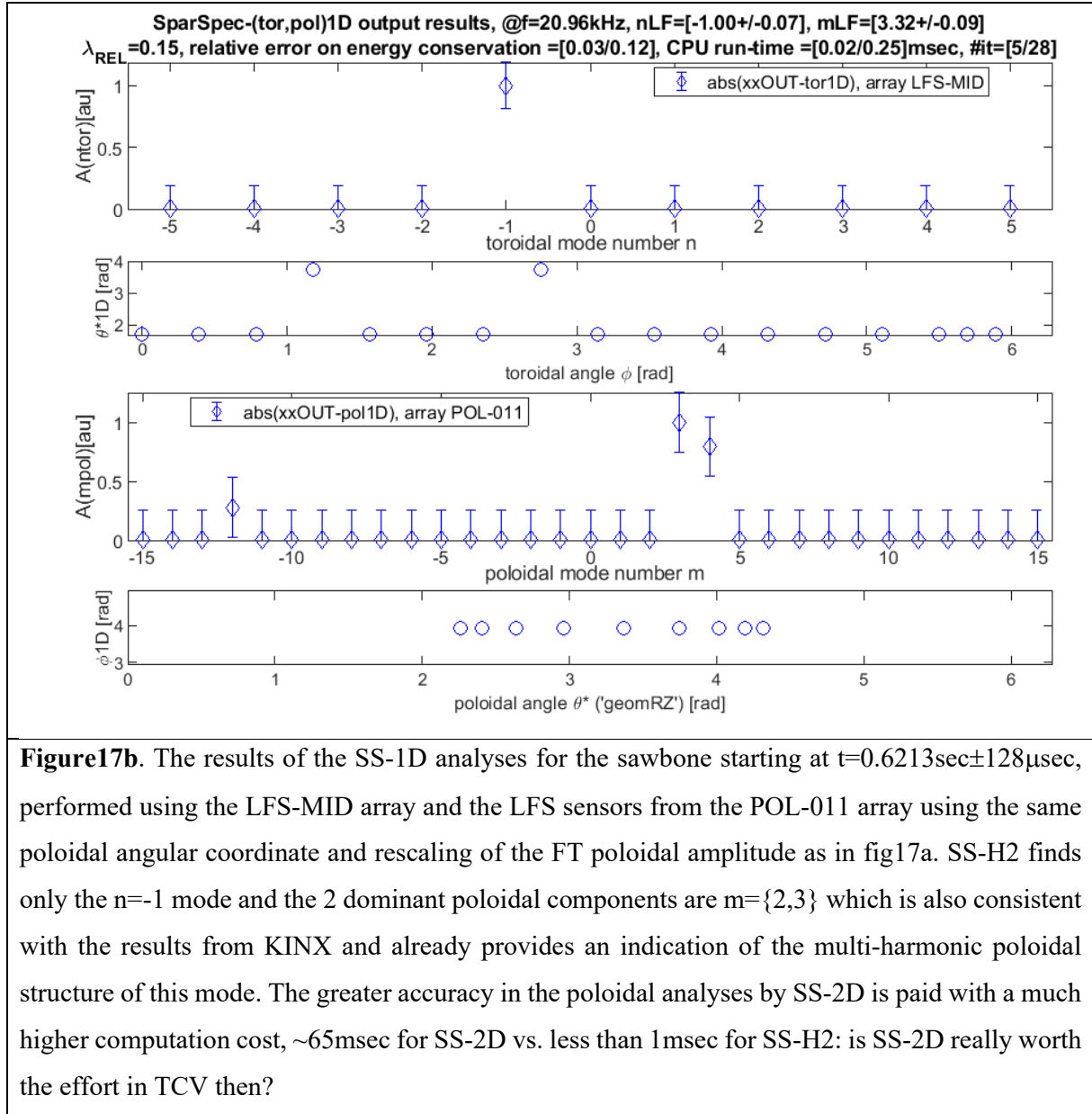


Figure18, D.Testa, J.Charrière, paper SparSpec2D-V1

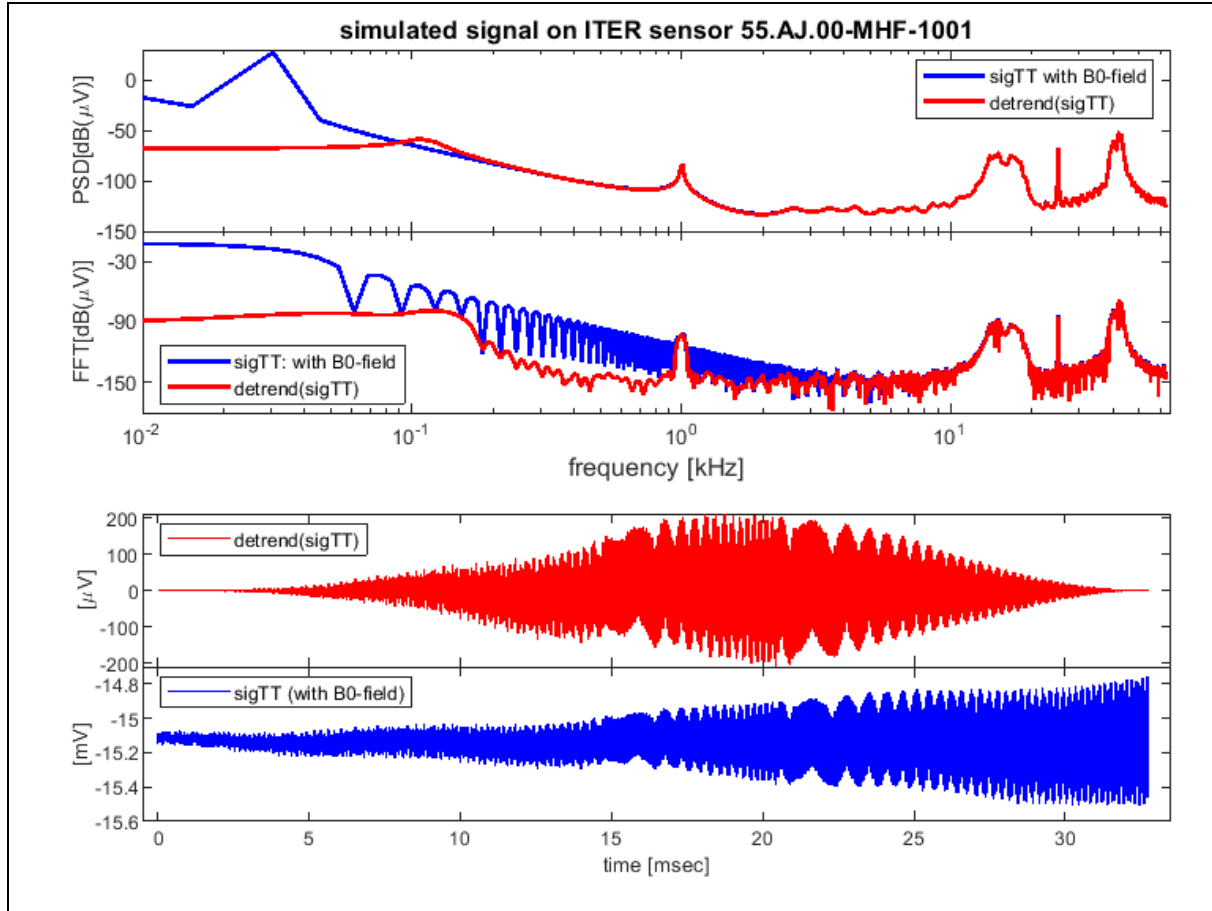


Figure18. The time trace and the frequency spectrum for one simulation and for one of the sensors considered in our ITER analyses. The input signal sigTT includes the poloidal equilibrium field B0, that is assumed to have been rectified by the vessel at 30Hz, and the 1kHz chopping frequency used by the DAQ to separate the slow acquisition (used for equilibrium analyses and RT control) from the fast acquisition at 2MHz (used for MHD analyses, both on-line and off-line). Following the nomenclature in [29], a background continuum Kolmogorov power spectrum, i.e. such that $\text{power} \propto \text{frequency}^{-5/3}$, and pink noise are used to pollute sigTT. There are three input modes, all with slowly varying frequency and amplitude over the $\sim 35\text{msec}$ time window of this simulation. The traces in red show the (frequency analysis of the) detrended sigTT, i.e. after software removal of B0. For the frequency analysis, and for illustrative purposes, we compare the FFT vs. the PSD spectrum evaluated over the entire time window of the simulation. The latter is evidently much cleaner and therefore more suitable to identify the individual frequency components, some of which are indeed the input Eigenmodes.

Figure19, D.Testa, J.Charrière, paper SparSpec2D-V1

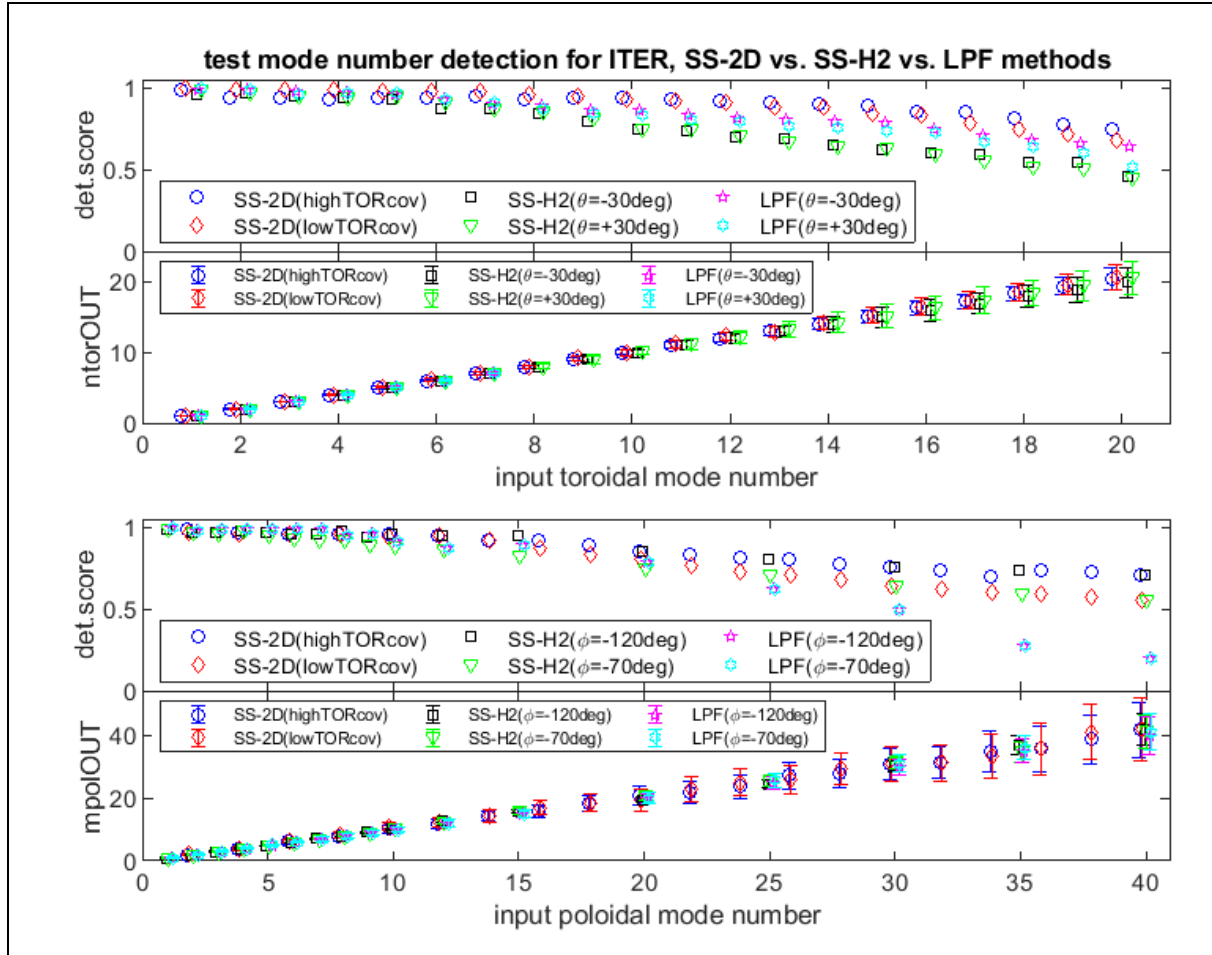


Figure19. The expected detection uncertainties for the toroidal and poloidal mode numbers used in the simulated ITER cases considered here, where we use the frequency-independent nominal values $\{\max(\sigma_k)=0.15, 10\text{deg}\}$ for the amplitude and phase measurement errors, respectively. These are nominal minimum values, namely each method cannot determine the mode numbers to better than the accuracy reported in this graph given the measurement uncertainties on the input (calibrated) magnetic data. The analysis is performed running 1'000 simulations with randomly generated amplitude and phase errors, always using for simplicity the pair of mode numbers $\{m,n\}$ such that $m=n \times q_{\text{res}}$, with $q_{\text{res}}=2$ in this case. We note that SS-2D out-performs the 1D methods for higher toroidal mode numbers, simply because for the selected groups of sensors there is not an ignorable coordinate, thus the phase differences along the coordinate orthogonal to the intended measurement axis can only be correctly dealt with by a 2D method.

Figure20, D.Testa, J.Charrière, paper SparSpec2D-V1

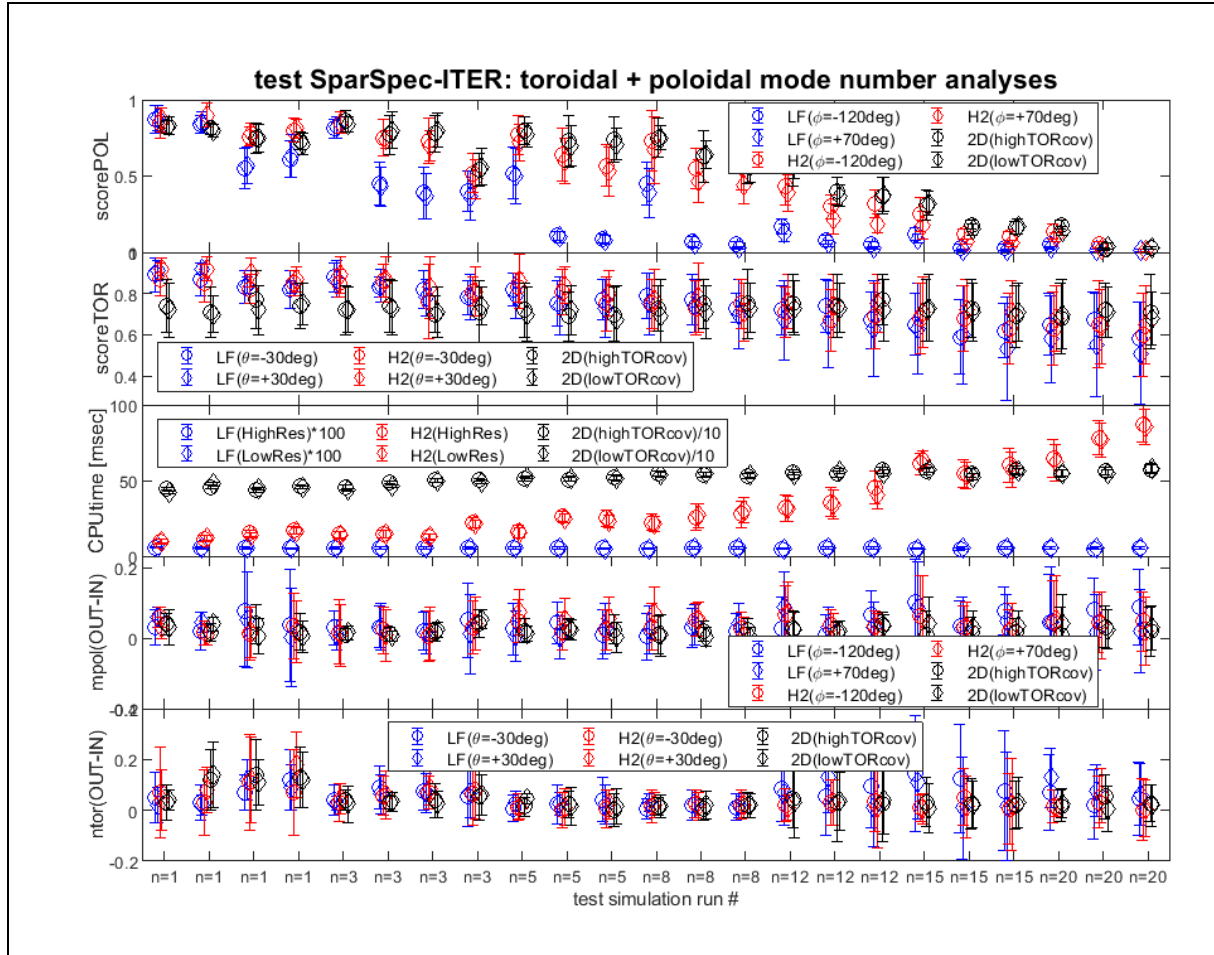


Figure20. The relative error, overall CPU run-time and simulation score for toroidal and poloidal mode number detection using the selected sets of magnetic sensors in ITER. The toroidal array at $\theta=+30\text{deg}$ and the poloidal array at $\phi=-70\text{deg}$ do not have high-resolution sensors, and are thus combined to give the *LowRes* results for the estimation of the overall CPU run-time, while the toroidal array at $\theta=-30\text{deg}$ and the poloidal array at $\phi=-120\text{deg}$ have high-resolution sensors and are then combined to give the *HighRes* results. The 23 test cases for which the results are reported here are labelled by the input toroidal mode number in the simulations, and for the same n_{TORIN} a different poloidal spectrum is used: the exact correspondence between is reported in Table3. The variable plotted is the rms value over all the 100x simulations performed for each test case, with the error bar representing the scatter (estimated by the standard deviation) around the central result.

Table1, D.Testa, J.Charrière, paper SparSpec2D-V1

shot	t ₀ [sec]	f ₀ [kHz]	n _{LF}	n _{H2}	n _{2D}	m _{LF}	m _{H2}	m _{2D}
49384	2.65	83.25	3.07±0.10	3, A=0.85	3, A=0.83	5.43±0.27	5, A=0.63 6, A=0.57 7, A=0.33 8, A=0.25	5, A=0.52 6, A=0.69 7, A=0.23 8, A=0.29
49384	2.65	88.37	4.12±0.08	4, A=0.82	4, A=0.85	6.78±0.42	6, A=0.61 7, A=0.48 8, A=0.54	5, A=0.50 6, A=0.49 7, A=0.51 8, A=0.27 9, A=0.81
49384	2.65	92.85	4.96±0.12	5, A=0.87	5, A=0.79	8.27±0.45	8, A=0.65 9, A=0.56 10, A=0.40	8, A=0.81 9, A=0.41 10, A=0.23
49384	2.65	92.85	4.96±0.12	5, A=0.83	5, A=0.85	8.27±0.45	0, A=0.65 4, A=0.49 8, A=0.29 17, A=0.38	0, A=0.59 4, A=0.50 13, A=0.35 23, A=0.27 25, A=0.29
49384	2.85	101.27	3.05±0.08	3, A=0.88	3, A=0.78	5.66±0.54	5, A=0.54 6, A=0.59 7, A=0.38 8, A=0.31	5, A=0.50 6, A=0.64 7, A=0.31 8, A=0.36
49384	2.85	106.04	4.15±0.15	4, A=0.92	4, A=0.84	7.12±0.48	6, A=0.25 7, A=0.57 8, A=0.62 9, A=0.34	7, A=0.77 8, A=0.36 9, A=0.37 10, A=0.17
49384	2.85	112.45	5.06±0.08	5, A=0.77	5, A=0.82	8.35±0.37	8, A=0.54 9, A=0.66 10, A=0.27 11, A=0.29	8, A=0.39 9, A=0.45 10, A=0.54 11, A=0.43 12, A=0.22
49384	3.25	110.23	3.13±0.13	3, A=0.82	3, A=0.83	5.43±0.54	6, A=0.67 7, A=0.44 8, A=0.50	5, A=0.27 6, A=0.50 7, A=0.53 8, A=0.51
49384	3.25	117.45	4.06±0.09	4, A=0.78	4, A=0.84	6.77±0.37	7, A=0.31 8, A=0.40 9, A=0.52 10, A=0.60	7, A=0.40 8, A=0.50 9, A=0.46 10, A=0.52
49384	3.25	124.87	5.14±0.06	5, A=0.82	5, A=0.75	8.49±0.40	8, A=0.49 9, A=0.49 10, A=0.39 11, A=0.35 12, A=0.37	8, A=0.53 9, A=0.59 10, A=0.44 11, A=0.25 12, A=0.17

Table2, D.Testa, J.Charrière, paper SparSpec2D-V1

shot	time [sec]	freq. [kHz]	n lin. fit	n SS-H2	n SS-2D	m lin. fit	m SS-H2	m SS-2D
55604	3.55	47.23	4.05±0.07	4, A=0.88	4, A=0.83	8.12±0.35	8, A=0.72 9, A=0.60	8, A=0.79 9, A=0.62
55604	3.60	60.12	4.12±0.05	4, A=0.78	4, A=0.83	8.09±0.29	7, A=0.62 8, A=0.47 9, A=0.53	8, A=0.74 9, A=0.58 10, A=0.43
55604	3.65	74.76	4.07±0.012	4, A=0.82	4, A=0.87	8.23±0.48	8, A=0.86	8, A=0.68 9, A=0.65
55604	3.90	50.23	3.12±0.12	3, A=0.87	3, A=0.85	6.07±0.54	5, A=0.67 6, A=0.69	5, A=0.58 6, A=0.63 7, A=0.40
55604	4.00	75.23	2.98±0.13	3, A=0.82	3, A=0.84	6.23±0.49	5, A=0.57 6, A=0.54 7, A=0.49	6, A=0.70 7, A=0.64 8, A=0.57
55604	4.05	87.54	3.15±0.05	3, A=0.78	3, A=0.88	6.14±0.32	6, A=0.72 7, A=0.58	5, A=0.54 6, A=0.52 7, A=0.53
55604	4.10	93.37	3.08±0.05	3, A=0.81	3, A=0.82	6.23±0.45	5, A=0.67 6, A=0.45 7, A=0.42	6, A=0.62 7, A=0.70 8, A=0.62
55604	4.20	51.12	2.87±0.27	2, A=0.79	2, A=0.75	4.12±0.36	4, A=0.67 5, A=0.64	4, A=0.62 5, A=0.54 6, A=0.36
55604	4.30	65.35	2.49±0.23	2, A=0.81	2, A=0.78	4.15±0.40	4, A=0.48 5, A=0.63 6, A=0.54	4, A=0.59 5, A=0.54 6, A=0.44
55604	4.40	85.38	2.15±0.13	2, A=0.83	2, A=0.87	4.23±0.42	4, A=0.67 5, A=0.67	4, A=0.75 5, A=0.59 6, A=0.45
55604	4.50	91.23	2.05±0.15	2, A=0.75	2, A=0.82	4.12±0.43	4, A=0.50 5, A=0.52 6, A=0.59	4, A=0.79 5, A=0.53 6, A=0.43
55604	4.50	91.23	2.05±0.15	2, A=0.75	2, A=0.82	4.12±0.52	0, A=0.70 3, A=0.32 11, A=0.27 35, A=0.32 37, A=0.14	0, A=0.73 2, A=0.17 4, A=0.28 18, A=0.25 25, A=0.32

Legend for Table1 and Table2, D.Testa, J.Charrière, paper SparSpec2D-V1

Table1. The toroidal and poloidal mode numbers calculated separately using the linear phase fit method ($=\{n,m\}_{LF}$) and 2xSS-H2 ($=\{n,m\}_{H2}$) vs. concurrently using SS-2D ($\{n,m\}_{2D}$). For the separate toroidal and poloidal analyses, the subset of sensors [H301, H302, H303, H304, H305] and [H304, H305, H306, H307] were separately used, respectively. Note that for the TAE modes in #49384 the poloidal mode number is always scaled by the nearest (towards zero) integer to the value of q_{LCFS} . In *italic* one example of the results of the 2xSS-H2 and SS-2D analyses performed using the currently surviving set of H30N magnetic sensors [H302, H303, H304, H305]. While it is clear that SS-2D provides results which are consistent with our theoretical understanding of TAE modes, in this particular instance these are not necessarily more accurate than those from 2xSS-H2, but they need a much more intensive CPU and RAM usage. When using the currently available reduced subset of H30N sensors, the toroidal mode numbers are correctly detected by SS-H2 and SS-2D, but the poloidal mode numbers are most definitively wrong.

Table2. As in Table1 but for #55064. Note that here the poloidal mode number is NOT scaled by the nearest (towards zero) integer to the value of q_{LCFS} . The result are essentials the same: it is clear that while TAEs have multiple poloidal harmonics, and are subject to toroidicity effects since are more localised modes, ACs are global modes characterised by a single dominant poloidal harmonic, and thus are much less sensitive to the toroidicity effects that would make the poloidal mode content at the wall, i.e. as measured by the magnetic sensors, different from that at the resonant q-surface: $q_{RES}=m/n=q_{MIN}$ for ACs, while $q_{RES}=(2m+1)/2n$ for TAEs.

Table3, D.Testa, J.Charrière, paper SparSpec2D-V1

ntorIN	mpolIN	A(au)	<mpolIN>	max. σ_{IN} for ntorIN	max. σ_{IN} for mpolIN
1	1	1	1.00	0.35	0.35
1	2	1	2.00	0.35	0.38
1	1 to 4	0.10;0.25;0.35;0.30	3.00	0.35	0.49
1	3;4;5	0.15;0.70;0.15	4.00	0.35	0.62
3	5	1	5.00	0.35	0.75
3	10;11;12	0.10;0.70;0.20	11.10	0.35	1.58
3	10;11;12	0.30;0.35;0.35	11.00	0.35	1.58
3	11 to 15	rand: >0.10 & <0.30	11.96	0.35	1.72
5	10;11	0.50;0.50	10.50	0.38	1.50
5	21 to 25	0.20 (each)	23.00	0.38	3.20
5	21 to 25	rand: >0.10 & <0.30	22.53	0.38	3.20
8	16;17	0.50;0.50	16.50	0.59	2.25
8	36 to 40	0.20 (each)	38.00	0.59	5.45
8	36 to 40	rand: >0.10 & <0.30	37.97	0.59	5.45
12	24;25	0.50;0.50	24.50	0.86	3.54
12	51 to 55	0.20 (each)	53.00	0.86	7.50
12	51 to 55	rand: >0.10 & <0.30	53.26	0.86	7.50
15	30;31	0.50;0.50	30.50	1.07	4.35
15	66 to 70	0.20 (each)	68.00	1.07	9.80
15	66 to 70	rand: >0.10 & <0.30	67.56	1.07	8.80
20	40;41	0.50;0.50	40.50	1.42	5.70
20	86 to 90	0.20 (each)	88.00	1.42	12.50
20	86 to 90	rand: >0.10 & <0.30	87.65	1.42	12.50

Table3. The input parameters for the simulations used to determine the {toroidal, poloidal} mode number detection score for the SS-2D vs. SS-H2 vs. the LPF methods for the selected groups of ITER magnetic sensors. Here A is the relative mode amplitude for each poloidal component for the single toroidal mode, normalized such that $\sum_k A_k^2=1$, and <mpolIN> is the average value of mpolIN over all the 20x simulations run for each toroidal mode, $\langle \text{mpolIN} \rangle = \sum_k \text{mpolIN}_k \sum_k A_k^2 / \sum_k A_k^2$.